



## An Intercomparison of Drought Indicators Based on Thermal Remote Sensing and NLDAS-2 Simulations with U.S. Drought Monitor Classifications

MARTHA C. ANDERSON,\* CHRISTOPHER HAIN,<sup>+</sup> JASON OTKIN,<sup>#</sup> XIWU ZHAN,<sup>@</sup> KINGTSE MO,<sup>&</sup>  
MARK SVOBODA,\*\* BRIAN WARDLOW,\*\* AND AGUSTIN PIMSTEIN<sup>++</sup>

\* *Hydrology and Remote Sensing Laboratory, Agricultural Research Service, USDA, Beltsville, Maryland*

<sup>+</sup> *Earth System Science Interdisciplinary Center, University of Maryland, College Park, College Park, Maryland*

<sup>#</sup> *Cooperative Institute for Meteorological Satellite Studies, University of Wisconsin—Madison, Madison, Wisconsin*

<sup>@</sup> *Center for Satellite Applications and Research, NOAA/NESDIS, College Park, Maryland*

<sup>&</sup> *NOAA/CPC, College Park, Maryland*

\*\* *National Drought Mitigation Center, University of Nebraska, Lincoln, Nebraska*

<sup>++</sup> *Pontificia Universidad Católica de Chile, Santiago, Chile*

(Manuscript received 24 September 2012, in final form 29 January 2013)

### ABSTRACT

Comparison of multiple hydrologic indicators, derived from independent data sources and modeling approaches, may improve confidence in signals of emerging drought, particularly during periods of rapid onset. This paper compares the evaporative stress index (ESI)—a diagnostic fast-response indicator describing evapotranspiration (ET) deficits derived within a thermal remote sensing energy balance framework—with prognostic estimates of soil moisture (SM), ET, and runoff anomalies generated with the North American Land Data Assimilation System (NLDAS). Widely used empirical indices based on thermal remote sensing [vegetation health index (VHI)] and precipitation percentiles [standardized precipitation index (SPI)] were also included to assess relative performance. Spatial and temporal correlations computed between indices over the contiguous United States were compared with historical drought classifications recorded in the U.S. Drought Monitor (USDM). Based on correlation results, improved forms for the ESI were identified, incorporating a Penman–Monteith reference ET scaling flux and implementing a temporal smoothing algorithm at the pixel level. Of all indices evaluated, anomalies in the NLDAS ensemble-averaged SM provided the highest correlations with USDM drought classes, while the ESI yielded the best performance of the remote sensing indices. The VHI provided reasonable correlations, except under conditions of energy-limited vegetation growth during the cold season and at high latitudes. Change indices computed from ESI and SM time series agree well, and in combination offer a good indicator of change in drought severity class in the USDM, often preceding USDM class deterioration by several weeks. Results suggest that a merged ESI–SM change indicator may provide valuable early warning of rapidly evolving “flash drought” conditions.

### 1. Introduction

Drought monitoring is a complex and multifaceted endeavor, warranting use of multiple tools. Drought impacts can be manifested in all components of the hydrologic budget: in water supply terms (precipitation), in storage (soil moisture, snowpack, groundwater, and surface water), and in exchange or flux terms (evapotranspiration, snowmelt, drainage/recharge, runoff, and streamflow). Each of these components has relevance to

specific groups of stakeholders, and each has a unique natural time scale of evolution. The current strategy in operational drought monitoring is to assemble a suite of independent indicators, sampling different types of relevant impacts at different temporal scales, and then to blend these indicators into a concise, integrated report using both subjective and objective approaches. This is the strategy used to construct the U.S. Drought Monitor (USDM; Svoboda et al. 2002), the primary record of drought classification for the United States since 1999. Lacking an absolute standard of “truth” in drought severity classification at continental scales, the USDM authors rely on a convergence of evidence between independent indicators, reported impacts, and expert

Corresponding author address: M. C. Anderson, Agricultural Research Service, USDA, 10300 Baltimore Ave., Beltsville, MD 20705.

E-mail: martha.anderson@ars.usda.gov

guidance from the field to determine the significance of emerging drought patterns.

To optimally synthesize signals from multiple drought indicators, their relative strengths and weaknesses must be well understood, as well as the unique information each one provides. Indices based on surface measurements are strongly tied to observations, but may have limits in spatial sampling and portability to other domains that lack dense in situ monitoring networks. Prognostic land surface models (LSMs) can provide quantitative estimates of a full suite of hydrologic variables, adding value to the precipitation data used as a primary input. However, model output may have significant biases because of inaccurate modeling assumptions, observational errors in the forcing data, and a reliance on surface parameter fields (e.g., soil texture and plant rooting depth) that may not be available with the required accuracy or spatial resolution (Betts et al. 1997; Schaake et al. 2004; Mo et al. 2012). Because they are principally constrained by the accuracy of the precipitation inputs, LSMs are typically limited in spatial resolution (several kilometers or coarser) and are only moderately portable to regions with sparse ground-based rain gauge networks required for accurate calibration. In comparison, diagnostic indicators based on satellite remote sensing can be generated at higher spatial resolution and with broad geographic coverage, but may have temporal sampling constraints, both in frequency and period of record. Data assimilation strategies have been developed to integrate in situ and remote sensing data into LSMs to reduce impacts of input biases and model parameterization errors (Houborg et al. 2012; Hain et al. 2012; Sheffield et al. 2012). This will likely be the optimal solution for future global drought monitoring efforts, providing a time-continuous suite of hydrologic variables generated from a unified modeling system or ensemble of systems. In preparation, intercomparisons between prognostic and diagnostic indicators provide insight regarding relative regional and seasonal performance.

This study focuses on diagnostic remote sensing indicators that are responsive to short-term environmental changes, since early warning capabilities are limited in current drought monitoring systems such as the USDM. Recent “flash drought” events, where surface moisture conditions declined rapidly because of high temperatures and enhanced evaporative losses, have highlighted the need for rapid response indicators. Vegetation cover condition, as sampled by remotely sensed shortwave vegetation indices (VIs), is a relatively slow response variable, typically adjusting only after notable crop damage has already occurred. Remote sensing indices based primarily on VI data include the vegetation drought response index (VegDRI; Brown et al. 2008) and the Moderate Resolution Imaging Spectroradiometer (MODIS)-based

drought severity index (Mu et al. 2013). In contrast, land surface temperature (LST) is a rapid response variable, and it can be readily sampled over a range in spatial resolution—from field to continental scales—using thermal infrared (TIR) satellite imagery. Drought signals in LST are conveyed by increases in soil and canopy temperatures as soil moisture deficits and vegetation stress develop and, in some cases, prior to reductions in VIs. Drought indicators based on LST include the vegetation health index (VHI; Kogan 1997), generated from empirical combinations of LST and VI data, and the evaporative stress index (ESI; Anderson et al. 2011), which combines LST and vegetation cover amount in an estimate of evapotranspiration (ET) computed within the context of a surface energy balance model. ET-based indicators, quantifying anomalous rates of water use or loss, may be uniquely sensitive to rapidly changing conditions relating to flash drought.

In this paper, ESI performance over the contiguous United States (CONUS) is compared with soil moisture (SM), ET, and runoff indices generated with the prognostic LSMs in the North American Land Data Assimilation System (NLDAS; Xia et al. 2012a,b) operated by the Environmental Modeling Center (EMC) at the National Centers for Environmental Prediction (NCEP) and used in the North American Drought Briefings (NADB; [www.cpc.ncep.noaa.gov/products/Drought](http://www.cpc.ncep.noaa.gov/products/Drought)). Also included in the intercomparison are standard drought indicators such as the VHI and the standardized precipitation index (SPI), an index based solely on precipitation observations. The performance of each indicator is assessed in comparison with retrospective drought classifications in the USDM from 2000 to 2011. These comparisons are used in two ways: first to confirm the realism of experimental drought products, and then to demonstrate cases where these products can anticipate droughts that later appear in the USDM. The goals of the study are to identify an optimal ESI form for real-time delivery and integration into the NADB and USDM, to better understand ESI performance in comparison with standard precipitation-based indicators, and to explore the role of diagnostic indicators as an independent assessment of drought signals conveyed by prognostic modeling systems. First-order time changes in ESI and NLDAS SM are also compared with changes in USDM drought classes to investigate synergistic utility for early identification of areas with rapidly intensifying agricultural drought conditions.

## 2. Data

### a. Evaporative stress index

The ESI represents standardized anomalies in a normalized clear-sky ET ratio,  $ET/F_{\text{ref}}$ , where  $F_{\text{ref}}$  is a scaling

flux used to minimize impacts of nonmoisture related drivers on ET (e.g., seasonal variations in radiation load). In previous studies (Anderson et al. 2007b, 2011), a modified Priestley–Taylor (Priestley and Taylor 1972) estimate of potential ET (PET) has been used as the normalization factor to compute the ESI. Here, the performance of several forms of scaling flux is examined, as well as a benchmark case using no scaling flux, sampling anomalies in ET itself.

ET estimates employed in the ESI are obtained from the TIR-based remote sensing Atmosphere–Land Exchange Inverse (ALEXI) model (Anderson et al. 1997; Mecikalski et al. 1999; Anderson et al. 2007a). ALEXI uses measurements of the morning LST rise, provided by geostationary satellites, as the main diagnostic input to a two-source (soil + vegetation) model of surface energy balance. Anderson et al. (1997) demonstrated that use of a time-differential LST signal reduces model sensitivity to errors in the absolute temperature retrieval. Because ALEXI is dependent on LST, direct ET retrievals can be achieved only under clear-sky conditions, although methods for gap-filling cloudy days have been developed (Anderson et al. 2007a, 2012). The ESI is formed from time composites of clear-sky  $ET/F_{ref}$  retrieved near local noon. Time compositing over periods of 1 week to several months serves to fill cloud-induced gaps in the model grid and to reduce noise due primarily to incomplete cloud clearing. It is hypothesized that use of clear-sky ET retrievals (as opposed to all-sky estimates) results in better separation of soil moisture–induced controls on ET from drivers related to variable radiation load such as cloud cover.

ALEXI is executed daily over CONUS on an approximately 10-km grid (pixel dimension  $0.0899^\circ$ ). The model is forced with meteorological inputs from the North American Regional Reanalysis (NARR; Mesinger et al. 2006), while LST inputs are obtained from the Geostationary Operational Environmental Satellites (GOES), and leaf area index (LAI) is interpolated from the 8-day *Terra* MODIS product (MOD15A2). Importantly, ALEXI does not use precipitation data as input: surface moisture patterns are conveyed to the model in proxy by the LST signal. The ALEXI period of record is currently limited to the MODIS era (2000 and following), but can be extended back to the early 1980s using VI data from the Advanced Very High Resolution Radiometer (AVHRR) series flown by the National Oceanic and Atmospheric Administration (NOAA) and geostationary data from the International Satellite Cloud Climatology Project (ISCCP) B1 data rescue project (Knapp 2008). Snow-covered regions have been masked using the 24-km resolution Daily Northern Hemisphere Snow and Ice Analysis product distributed through the National Snow

and Ice Data Center (NSIDC; [http://nsidc.org/data/docs/noaa/g02156\\_ims\\_snow\\_ice\\_analysis/index.html](http://nsidc.org/data/docs/noaa/g02156_ims_snow_ice_analysis/index.html)). ESI composites were computed for 1-, 2-, and 3-month time scales (see section 3a). Standardized anomaly computations for transforming daily  $ET/F_{ref}$  time series into ESI are described in section 3b. Real-time ESI maps over CONUS during the growing season can be viewed at <http://hrsl.arsusda.gov/drought>.

### *b. North American Land Data Assimilation System*

ESI drought assessments have been compared with SM, ET, and runoff data from the North American Land Data Assimilation System–Phase 2 (NLDAS-2) maintained by NCEP, including output from three land surface modeling systems: Noah (Ek et al. 2003; Barlage et al. 2010; Livneh et al. 2010; Wei et al. 2013), Mosaic (Koster and Suarez 1994, 1996; Koster et al. 2000), and the Variable Infiltration Capacity (VIC) model (Liang et al. 1994, 1996; Bowling and Lettenmaier 2010). While all three LSMs model the surface energy and water balance, LST, and SM in multiple layers, their treatment of infiltration, drainage, rooting depth and canopy uptake, and soil evaporation differs, yielding regionally differential responses based on local climate, soils, and vegetation characteristics. Given this variability, previous studies of NLDAS-derived drought indicators suggest that ensemble averages of model output better depict drought conditions compared to output from individual modeling systems (Dirmeyer et al. 2006; Mo et al. 2011). Output from the Sacramento Soil Moisture Accounting (SAC-SMA) model (Burnash 1995), also incorporated in the NCEP NLDAS-2 configuration, is not included in this study because SAC-SMA does not implement a full energy balance and is conceptually less comparable to ALEXI.

The NCEP-NLDAS models are forced with the same NARR meteorological inputs (e.g., air temperature, wind, and vapor pressure) used by ALEXI. While this commonality introduces some interdependence, ALEXI is much less sensitive to meteorological forcings than to LST time difference inputs (Anderson et al. 1997). Precipitation analyses used in NLDAS are described by Xia et al. (2012b). Here we use output of monthly averaged total soil column SM and all-sky daily ET. Monthly SM percentiles have been computed with respect to a 30-yr climatology (1979–2008). SM data from individual models are referred to as  $SM_{NO}$  (Noah),  $SM_{MO}$  (Mosaic),  $SM_{VI}$  (VIC), and  $SM_{AV}$  (ensemble), and analogously for ET output. In addition, the standardized runoff index (SRI) computed for 3- and 6-month intervals from ensemble-averaged runoff values was included in the analysis.

Data over CONUS were provided on a  $0.125^\circ$  grid. For comparison with ESI, NLDAS SM, ET, and SRI data

have been renormalized to the ALEXI period of record, as described in section 3b.

### c. Standardized precipitation index

ESI and NLDAS drought indicators were also compared with the SPI (McKee et al. 1993, 1995), considered to be a standard in drought monitoring (Hayes et al. 2011). The SPI uses observed precipitation as the sole input. Precipitation data at a given location are fit to a distribution function and then transformed into a normal distribution based on a local long-term climatology. The SPI data are standardized such that a value of 0 indicates the median precipitation amount (in comparison with the climatology) was measured at that pixel over the time interval in question. The SPI can be computed over multiple intervals (typically ranging from 2 to 52 weeks) to monitor different time scales of drought.

Here, we use SPI computed over 3- and 6-month intervals using the NLDAS-2 precipitation dataset (Xia et al. 2012b), generated from a temporal disaggregation of a gauge-only Climate Prediction Center (CPC) analysis of daily precipitation and including an orographic adjustment based on the climatology of the Parameter-Elevation Regressions on Independent Slopes Model (PRISM; Daly et al. 1994) precipitation dataset. Data over CONUS were provided at monthly time steps on a 0.5° grid, referenced to baseline conditions over the period 1979–2008.

### d. Vegetation health index

As a comparison to the TIR-based ESI, the VHI (Kogan 1995) has been included in the analyses. VHI uses two of the primary remote sensing inputs to ALEXI: LST and vegetation cover amount (as quantified via a VI), but combined empirically rather than within a physical surface energy balance framework. The analyses will evaluate how well this simple approach performs in comparison with the more complex ESI and identify areas and times of major similarity and difference.

The VHI is a composite of normalized LST- and VI-based indices. The vegetation condition index (VCI) rescales the normalized difference vegetation index (NDVI) on a pixel-by-pixel basis, scaling between minimum and maximum values ( $NDVI_{\min}$  and  $NDVI_{\max}$ , respectively) observed at each pixel over a long temporal record since 1981:

$$VCI = \frac{NDVI' - NDVI_{\min}}{NDVI_{\max} - NDVI_{\min}}, \quad (1)$$

where  $NDVI'$  is the average NDVI observed over the compositing period of interest (e.g., week, month, or growing season). The temperature condition index (TCI)

is analogous, but it is based on climatologically normalized brightness temperatures (BT):

$$TCI = \frac{BT_{\max} - BT'}{BT_{\max} - BT_{\min}}. \quad (2)$$

The flip in sign between Eqs. (1) and (2) reflects the natural anticorrelation that tends to exist between LST and NDVI under moisture-limiting vegetation growth conditions, with lower cover regions tending to be hotter because of reduced transpiration rates and/or soil moisture.

Assuming an equal contribution of both VCI and TCI to the combined index, VHI is usually computed as the average of VCI and TCI:

$$VHI = 0.5VCI + 0.5VTI. \quad (3)$$

VHI is a standard global product generated weekly by NOAA using NDVI and BT data obtained from the NOAA-AVHRR sensor series. For this study, global VHI data at 0.1442° resolution were extracted over CONUS and flagged with the same NSIDC snow cover product that was applied to ALEXI.

### e. U.S. Drought Monitor

Through expert analysis, authors of the weekly USDM report subjectively integrate information from many existing drought indicators along with local reports from state climatologists and observers across the country (Svoboda et al. 2002). The USDM is unique among the drought indices studied here because it includes drought information at multiple time scales, as well as socioeconomic considerations. While the USDM should not be considered an absolute metric of truth in drought monitoring, it is useful as a benchmark for assessing the spatiotemporal response of different drought indices.

The weekly USDM is a “composite indicator,” combining several variables into a single product that attempts to show both short- (S) and long-term (L) drought on one map. Variables (indices and indicators) utilized in the process address precipitation, temperature, vegetation health, soil moisture (modeled and in situ where available), streamflow, snowpack, snow water equivalent, reservoirs, and groundwater. The USDM is also unique in that it incorporates feedback and input into the process by maintaining and utilizing an expert user group of around 350 people in the field who serve as a “ground truth” to the product. A convergence of evidence approach is used to combine the scientific data with impacts and feedback from experts in the field via an iterative process.

The underlying backbone of the USDM is utilization of a ranking percentile approach, which gives historical

context to any given value/score by defining the percentage of scores in the associated frequency distribution that are of the same or lower value. The classification schema/categories run from D0–D4, with D0 equaling “abnormally dry” (D0 = 30th percentile) conditions. Moderate drought (D1 = 20th percentile) is the first designated level of drought, and severe (D2 = 10th percentile), extreme (D3 = 5th percentile), and exceptional (D4 = 2nd percentile) round out the rest of the classification. This approach also allows for the evaluation and inclusion of new parameters as they come online.

The USDM process also generates a set of weekly composite objective blend drought indicator (OBDI) products that were developed by the USDM authors as an attempt to objectively show both short- and long-term drought as separate maps for those who wish to separate the two. The short-term objective blend drought indicator (stOBDI) currently consists of five inputs weighted accordingly after experimental trial and error runs over 18 months: Palmer Z index (35%), 1-month SPI (20%), 3-month SPI (25%), CPC Soil Moisture Model (13%), and the Palmer drought severity index (PDSI) (7%). The long-term OBDI (ltOBDI) consists of six inputs weighted accordingly: PDSI (25%), 24-month SPI (20%), 12-month SPI (20%), 6-month SPI (15%), 60-month SPI (10%), and the CPC Soil Moisture Model (10%). The CPC soil moisture dataset currently used in the USDM production is based on a one-layer leaky bucket model (Fan and van den Dool 2004). In addition, percentiles derived for NLDAS-2 top 1-m soil moisture, total soil column soil moisture, and total runoff have been ingested into the USDM as an overlay data stream since January 2010.

For this study, weekly USDM drought classification data for 2000–11 were provided in shapefile format by the National Drought Mitigation Center (NDMC) and rasterized onto the 10-km ALEXI grid. For computational purposes, the drought classes were mapped to numerical values (D0 = 0, D1 = 1, D2 = 2, D3 = 3, and D4 = 4) with “no drought” assigned a value of  $-1$ . Note that all classes of wet conditions are contained within the no drought class; thus, the distribution of USDM classes in temperate regions that experienced little drought over the period of record may be strongly skewed toward values of  $-1$ .

### 3. Methods

#### a. Temporal compositing

Individual datasets used in the analysis were obtained at different native time steps—daily (clear sky only) for ALEXI, weekly for USDM and VHI, and monthly for NLDAS—and at different spatial resolutions.

To standardize spatial and temporal sampling, weekly and monthly datasets were first regridded to the ALEXI grid using nearest-neighbor assignment, then distributed to daily sampling by assuming constant values at each given pixel over the prior week or month. All datasets were then composited to simulate average conditions over various time scales.

In this study, composites were generated at 28-day time steps (roughly monthly) over 4-, 8-, 12-, and 26-week (approximately 1-, 2-, 3-, and 6-month) moving windows (time stamped by the end date). The 26-week composite is essentially a growing season average for April through September, while the 4- to 12-week composites sample different phenological phases in vegetation development and different time scales of drought persistence. Composites were computed as an unweighted average of all index values over the interval in question:

$$\langle v(w, y, i, j) \rangle = \frac{1}{nc} \sum_{n=1}^{nc} v(n, y, i, j), \quad (4)$$

where  $\langle v(w, y, i, j) \rangle$  is the composite for week  $w$ , year  $y$ , and  $i, j$  grid location,  $v(n, y, i, j)$  is the value on day  $n$ , and  $nc$  is the number of days with good data during the compositing interval. Cloudy-day values in ALEXI are flagged and excluded from the composites.

#### b. Anomaly computations

Each normalized index (USDM, VHI, SPI, SRI, and SM) used in this study refers to climatological conditions defined over different periods of record. Use of longer climatologies tends to decrease the apparent severity of isolated drought events, placing them within a broader historical context. These differences can introduce complexity into index intercomparisons, as the definition of “normal” may vary from index to index.

In the analyses presented here, all indices including USDM drought classes have been rescaled to standardized anomalies computed with respect to the ALEXI period of record (2000–11). The rescaled indices are expressed as a pseudo  $z$  score, normalized to a mean of zero and a standard deviation of one. Fields describing normal (mean) conditions and temporal standard deviations at each pixel are generated for each compositing interval. Then standardized anomalies at pixel  $i, j$  for week  $w$  and year  $y$  are computed as

$$v(w, y, i, j)' = \frac{\langle v(w, y, i, j) \rangle - \frac{1}{ny} \sum_{y=1}^{ny} \langle v(w, y, i, j) \rangle}{\sigma(w, i, j)}, \quad (5)$$

where the second term in the numerator defines the normal field, averaged over all years  $ny$ , and the denominator

is the standard deviation. In this notation,  $ESI-X$  is defined as  $ET/F'_{ref}$  computed for an  $X$ -month composite, while  $ETI-X$  is defined as  $ET'$  (anomalies in unscaled  $ET$ ). The prime is dropped when denoting renormalized indices in the discussion below, but is implied unless otherwise noted.

### c. *ESI refinements*

Two refinements to the original  $ESI$  construction scheme (Anderson et al. 2007b, 2011) have been evaluated in this study: 1) use of alternate forms of scaling flux and 2) use of temporal smoothing at the pixel level to reduce noise, related primarily to incomplete cloud clearing.

#### 1) CHOICE OF SCALING FLUX

Use of a scaling flux is common in thermal remote sensing of  $ET$  for upscaling from instantaneous retrievals at the time of satellite overpass to daily total  $ET$  and for gap-filling cloudy days when  $LST$  cannot be measured using  $TIR$  data (Ryu et al. 2012; Delogu et al. 2012). This practice assumes temporal preservation of a dimensionless ratio that conveys information about the surface moisture status. Given scaled  $ET$  ratios computed at times of clear-sky satellite overpasses,  $ET$  can be reconstructed for intervening times using interpolated ratio values and hourly or daily estimates of the scaling flux (e.g., Allen et al. 2007; Anderson et al. 2012).

Here we test four different scaling fluxes  $F_{ref}$  that are commonly used in  $ET$  upscaling, spanning a range in computational complexity and data demand. These include two forms of potential or reference  $ET$ : the Penman–Monteith (PM) formulation, as codified in the Food and Agricultural Organization (FAO-56) standard (Allen et al. 1998), and the Priestley–Taylor (PT) equation (Priestley and Taylor 1972), which ignores advective contributions to the potential evaporative flux. Available energy (net radiation minus the soil heat flux) is also evaluated as a scaling flux, resulting in a ratio termed the evaporative fraction (EF). Finally, the simplest case using only insolation (SDN) to scale  $ET$  is tested. The resulting  $ET/F_{ref}$  ratios will be denoted  $f_{PM}$ ,  $f_{PT}$ ,  $f_{EF}$ , and  $f_{SDN}$ , respectively. These cases are contrasted with anomalies computed using no scaling flux ( $f_0$ ).

#### 2) TEMPORAL SMOOTHING

Anderson et al. (2007b, 2011) used time composites of raw scaled  $ET$  values in Eq. (5) to compute  $ESI$ . However, incomplete screening of cloud-impacted  $LST$  inputs to ALEXI can serve to either increase or decrease the  $LST$  rise signal, depending on whether the clouds occur in the early morning or near noon, respectively. This leads to spurious reductions or enhancements of

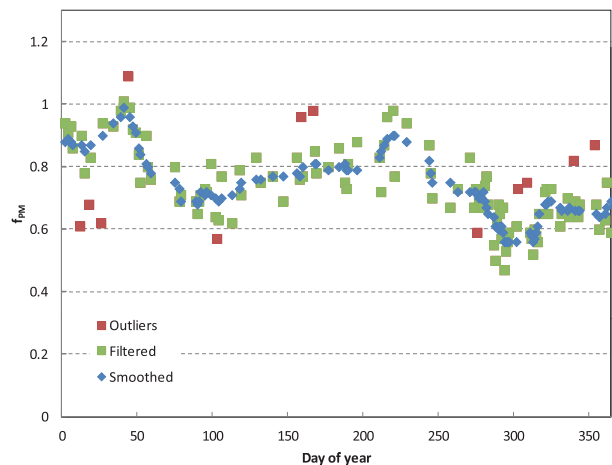


FIG. 1. Example of time series smoothing applied to  $f_{PM}$  extracted at a grid point in GA (see Fig. 2) for the year 2010. Red data points are screened outliers. The remaining filtered points (green) are processed with a Savitzky–Golay filter to produce the smoothed time series (blue).

$ET$  retrievals from the ALEXI algorithm and will add noise to the  $ET/F_{ref}$  composites. While GOES-derived cloud masks are implemented in the ALEXI processing infrastructure, thin clouds, particularly in the early morning, are notoriously difficult to detect (Schreiner et al. 2007). Here, a smoothing methodology is tested that exploits the dense time series of information available from geostationary satellites to reduce random day-to-day noise in  $ET/F_{ref}$  and to identify and screen data points influenced by clouds prior to compositing.

An example of the smoothing approach is shown in Fig. 1, as applied to a grid cell located in the state of Georgia (see Fig. 2). The algorithm first filters time series of the scaled flux, searching for and eliminating isolated outliers that do not follow recent trends in  $ET/F_{ref}$ . The assumption is that any abrupt SM-induced change in  $ET$  ratio is likely to persist for several days, while isolated outliers are likely cloud related. The algorithm iteratively identifies and screens points that exceed a  $\pm 2$  standard deviation ( $\sigma$ ) threshold computed within a moving window of width  $\pm 7$  points around the point in question. Next, the remaining points are smoothed with a Savitzky–Golay (Savitzky and Golay 1964) filter employing a second-order smoothing polynomial. The algorithm outputs temporally smoothed map grids, sampled only at pixels that had a valid, unscreened clear-sky retrieval on any given day. These grids are input to the compositing and anomaly computation algorithms described above.

### d. *Correlation analyses*

Following Anderson et al. (2011), drought indices were compared via temporal correlation as a function of

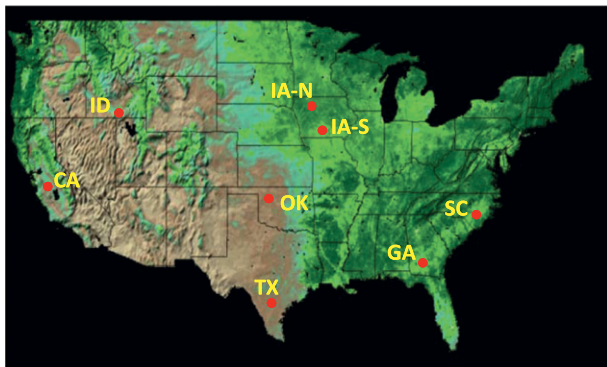


FIG. 2. Locations of sampling points used in intercomparisons. Colors in background indicate midseason vegetation cover fraction, ranging from 0 (brown) to 1 (dark green).

location across the domain and via spatial correlation as a function of time over the ALEXI period of record. Both assessments are limited in their ability to convey objective information about the performance of a single index pair because the correlation coefficient is impacted not only by index agreement, but also by the magnitude of variation in moisture conditions across the domain or through time. However, comparisons of correlations between multiple index pairs should provide a measure of relative compatibility.

For these correlation analyses, all indices except USDMM were convolved to the  $0.5^\circ$  resolution of the SPI products before computing the standardized anomalies. Average temporal and spatial correlations were computed using monthly maps from April to October to focus on growing season conditions, which tend to be more robustly captured by drought indicators and less affected by snow-cover masking. Spatial correlation time series were also computed for all months to identify seasonal trends in interindex agreement.

Statistics are reported in terms of the Pearson correlation coefficient, a measure of linear dependence between two variables. The Spearman nonparametric coefficient of rank correlation, which does not assume linear dependence, was also tested and yielded similar results in terms of ranking correlation strength between variables. Nonlinearities were particularly notable in the northeastern U.S. between USDMM class anomalies and other drought indicators because of skewness in the USDMM distribution, which does not sample “wetter than normal” conditions. While this nonlinearity tends to degrade temporal correlations in regions where “no drought” is a common occurrence, relative degree of correlation (correlation differences) at a given point in the domain still provides useful information as to whether index 1 is better at ranking USDMM drought classes than is index 2.

#### e. Change detection

The process of operational drought monitoring, as in the construction of USDMM maps, depends on accurately identifying areas with changing drought status. Typically, a USDMM author will start with the classification from the prior week and determine areas that require modification. To assist this process, we have created an ESI change product that tracks the significance of index changes over periods of 1–4 weeks. ESI change (denoted  $\Delta\text{ESI}$ ) is computed by differencing composites of smoothed  $\text{ET}/F_{\text{ref}}$ , then computing standardized anomalies in the difference products. This final step is valuable (in comparison with delivering simple differences between ESI products) because it brings maps at all change intervals to a common magnitude scale and highlights significance of change in comparison with climatology. Similar change products have been computed from the NLDAS ensemble-averaged SM anomalies.  $\Delta\text{ESI}$  and  $\Delta\text{SM}$  have been compared to changes in USDMM drought classifications to explore the utility of these change products in providing clear early warning in areas where soil moisture conditions are rapidly deteriorating.

## 4. Results and discussion

### a. Optimizing the ESI formulation

The impact of data smoothing and scaling flux selection was quantified in terms of average temporal and spatial correlation coefficient ( $r$ ) computed between different ESI forms, USDMM class anomalies, and NLDAS SM anomalies from all three LSMs and the ensemble average (Table 1). For both ESI and SM anomalies, time series of 4-week composites sampled at monthly intervals between April and October for the years 2000–11 were used in the correlation computations.

As evidenced in Table 1, the PM scaling flux  $\text{ESI}_{\text{PM}}$  provided the highest average spatial and temporal correlations with both USDMM and SM anomalies, while the unscaled ET (ETI) from ALEXI provided the lowest correlations. This suggests that scaling ET by any of the reference fluxes tested adds value by enhancing the ability of the index to discriminate moisture status. Of the soil moisture products, ESI correlates best with anomalies in  $\text{SM}_{\text{AV}}$ , followed by  $\text{SM}_{\text{VT}}$ . For all scaling fluxes, time series smoothing [as described in section 3c(2)] improved average correlations by approximately 0.04. For the sake of brevity, correlations with unsmoothed time series are shown in Table 1 only for the PM scaling flux.

Figure 3 provides insight into the relative efficacy of each scaling flux in removing normal seasonal variability from the  $\text{ET}/F_{\text{ref}}$  soil moisture proxy signal. These plots show annual time traces of  $f_0$ ,  $f_{\text{PM}}$ ,  $f_{\text{PT}}$ ,  $f_{\text{EF}}$ , and  $f_{\text{SDN}}$  for

TABLE 1. Average temporal and spatial correlation coefficients,  $\langle r \rangle$ , computed between ESI forms, soil moisture anomalies, and USDM class anomaly time series at sampled at 4-week intervals for April–October of 2000–11. Boldface indicates highest temporal and spatial correlation.

	Temporal correlations						Spatial correlations					
	ESI <sub>PM</sub>	ESI <sub>PM</sub> (unsmoothed)	ESI <sub>PT</sub>	ESI <sub>EF</sub>	ESI <sub>SDN</sub>	ETI	ESI <sub>PM</sub>	ESI <sub>PM</sub> (unsmoothed)	ESI <sub>PT</sub>	ESI <sub>EF</sub>	ESI <sub>SDN</sub>	ETI
USDM	<b>0.517</b>	0.483	0.493	0.464	0.453	0.445	<b>0.500</b>	0.462	0.474	0.441	0.438	0.431
SM <sub>NO</sub>	<b>0.640</b>	0.604	0.609	0.573	0.561	0.552	<b>0.608</b>	0.572	0.573	0.534	0.526	0.519
SM <sub>VI</sub>	<b>0.657</b>	0.618	0.622	0.580	0.568	0.559	<b>0.625</b>	0.586	0.585	0.543	0.533	0.526
SM <sub>MO</sub>	<b>0.617</b>	0.579	0.577	0.545	0.532	0.522	<b>0.577</b>	0.539	0.529	0.493	0.481	0.474
SM <sub>AV</sub>	<b>0.669</b>	0.630	0.632	0.593	0.580	0.570	<b>0.636</b>	0.596	0.592	0.551	0.540	0.532

example grid points in Georgia and Texas and two points in Iowa: one in northern Iowa in a region of high corn and soybean cropping density, and another in the southern part of the state with lower corn/soybean crop acreage (see Fig. 2). For all regions,  $f_{PM}$  results in the best relative separation between yearly traces, which are differentiated in part by variable SM conditions. The value of including the advective term in the Penman–Monteith equation, neglected in the Priestley–Taylor form for PET, can be noted by comparing ESI<sub>PM</sub> and ESI<sub>PT</sub> correlations in Table 1. Improvement in temporal correlation using the PM scaling flux is most pronounced over the eastern United States. All scaling fluxes serve to reduce seasonal variability in comparison with the unscaled case ( $f_0$ ).

Note in Fig. 3 that the ability of the scaling fluxes to remove seasonal variations differs between regions. The scaled flux curves are notably flattened in Georgia and Texas, but considerable seasonal variation remains at the Iowa sites, particularly for the dense corn/soybean cropping region in northern Iowa. In these areas, the ESI signal will partially reflect interannual changes in crop phenology, such as delayed planting and emergence because of cooler spring temperatures, which may not be related to anomalous SM conditions. The steep slopes of the curves at the northern Iowa site indicate that conditions are changing rapidly during the compositing interval, further obfuscating interpretation of composited values at various time scales.

Based on the results presented in this section, ESI computed from smoothed  $f_{PM}$  time series will be used in the following correlation analyses.

### b. Index intercomparison

#### 1) CLIMATOLOGICAL PATTERNS IN ET

Maps of seasonal means and standard deviations in several diagnostic and prognostic ET-based indicators included in this study are shown in Fig. 4, computed from 26-week composites over a nominal growing season period of April–September. Comparing mean values of

scaled ET indices ( $f_{PM}$ ,  $f_{PT}$ , and  $f_{EF}$ ) and  $f_0$  (unscaled ET) from ALEXI, it is evident that the scaling flux has reduced latitudinal gradients due to variations in solar radiation load, particularly in the eastern United States. Of these, the PM scaling flux  $f_{PM}$  generates the most uniform north–south distribution of mean index values.

Seasonal mean ET from ALEXI ( $f_0$ ) and NLDAS (ET<sub>NO</sub>, ET<sub>MO</sub>, ET<sub>VI</sub>, and ET<sub>AV</sub>) in general show similar patterns, although it should be remembered that  $f_0$  is based on clear-sky midday ET, while the NLDAS monthly ET includes impacts of cloud climatology. Of these, Mosaic generates the highest ET estimates, while the Noah LSM predicts lower ET in the northern United States along the Great Lakes, similar to findings by Xia et al. (2012b) for 28-yr mean annual evaporation estimates. They note that recalibration of VIC has removed overestimation of annual ET in the southeastern United States observed with NLDAS-1 (Mitchell et al. 2004); however, VIC now yields lower ET over the southeast with respect to other NLDAS-2 models during the growing season.

While normal mean conditions show similarity between ET indicators, maps of standard deviation in seasonal composites show that the various indices are characterized by significantly different patterns of variability. All indicate Texas as highly variable because of the strong drought events (in 2006 and 2011) and wetter conditions (2007) that occurred over the 2000–11 timeframe. Among NLDAS ET output, ET<sub>MO</sub> stands apart as having very different variability patterns, particularly along the lower Mississippi River basin where the standard deviation is high. In contrast ALEXI indices  $f_{PM}$ ,  $f_{PT}$ ,  $f_{EF}$ , and  $f_0$  show relatively low variability in this region, particularly in the evaporative fraction dataset. This is reasonable given the pervasiveness of irrigated agriculture and flooded rice paddies in combination with shallow water tables in the basin. More stable moisture conditions, because of local enhancements of nonprecipitation related moisture inputs like irrigation or extraction from shallow water tables, are implicitly captured by the diagnostic LST inputs to ALEXI but must be

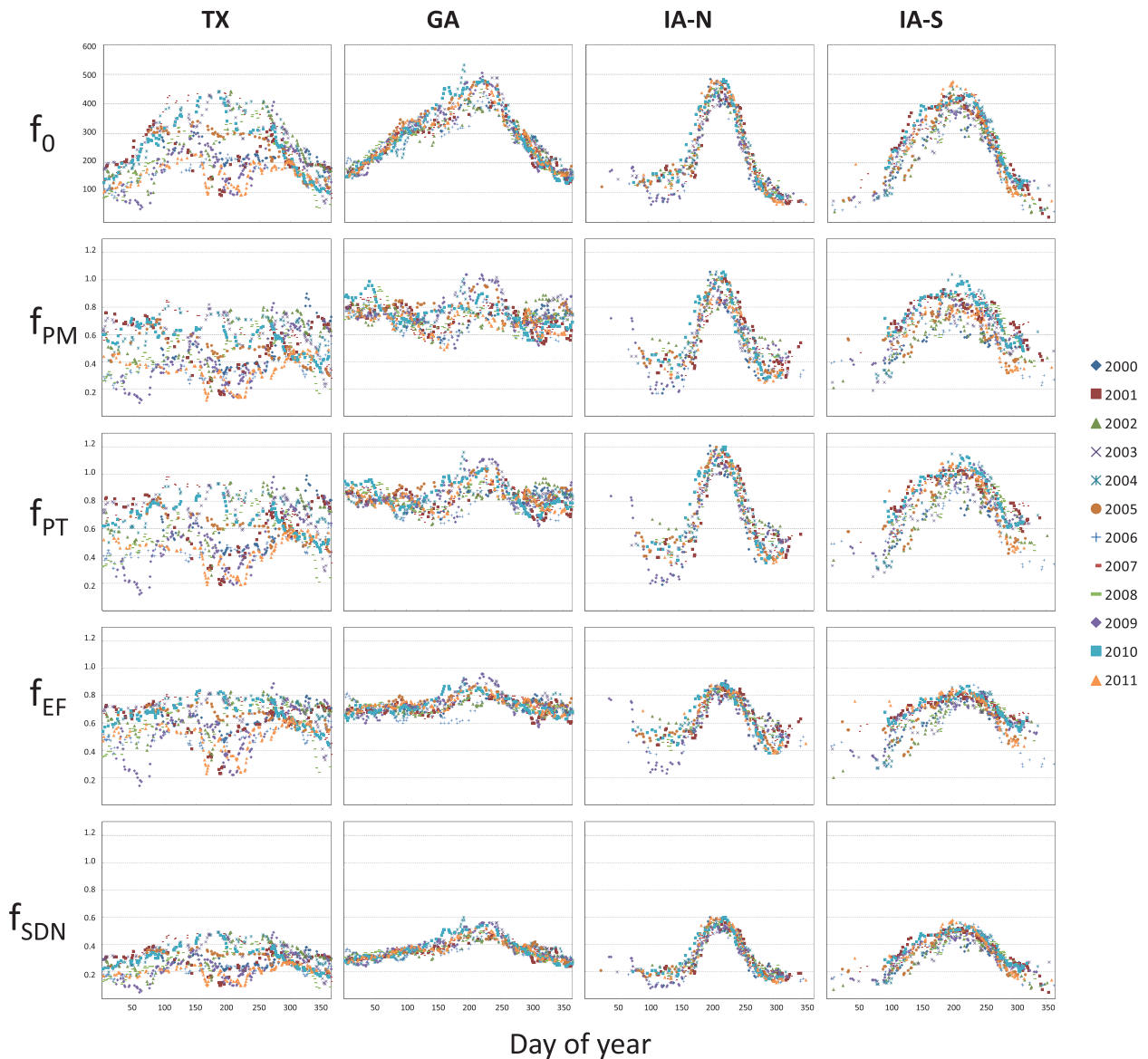


FIG. 3. Smoothed  $ET/F_{ref}$  time series for 2000–11, comparing several scaling fluxes ( $f_{PM}$ ,  $f_{PT}$ ,  $f_{EF}$ , and  $f_{SDN}$ ) and a benchmark case using no scaling ( $f_0$ ) ( $W m^{-2}$ ).

modeled explicitly in prognostic land surface modeling systems and are not currently represented in NCEP NLDAS-2 simulations. Drought resilience may also be impacted by plant rooting depth, which is difficult to accurately map a priori.

2) ANNUAL DROUGHT PATTERNS

Figure 5 compares drought maps composited over a nominal growing season (April–September) from select remote sensing and precipitation-based indicators with drought severity classes recorded in the USDM for 2000–11. In general, the major annual drought patterns are captured by each index at this coarse time scale. The

similarity between ESI and  $SM_{AV}$  is notable, given that these indices are constructed from completely independent signals—LST for ESI, and precipitation for  $SM_{AV}$ —and suggests that in combination they will provide strong evidence of emerging drought signals. While in most cases VHI is in agreement with other indicators, major differences are noted in 2000 and regional drought events are missed in 2001 (northeast) and 2008 (southeast).

3) MONTHLY TEMPORAL CORRELATIONS

While interindex correlations in drought patterns are strong at the annual scale, we start to note larger differences in response at shorter time scales. Average

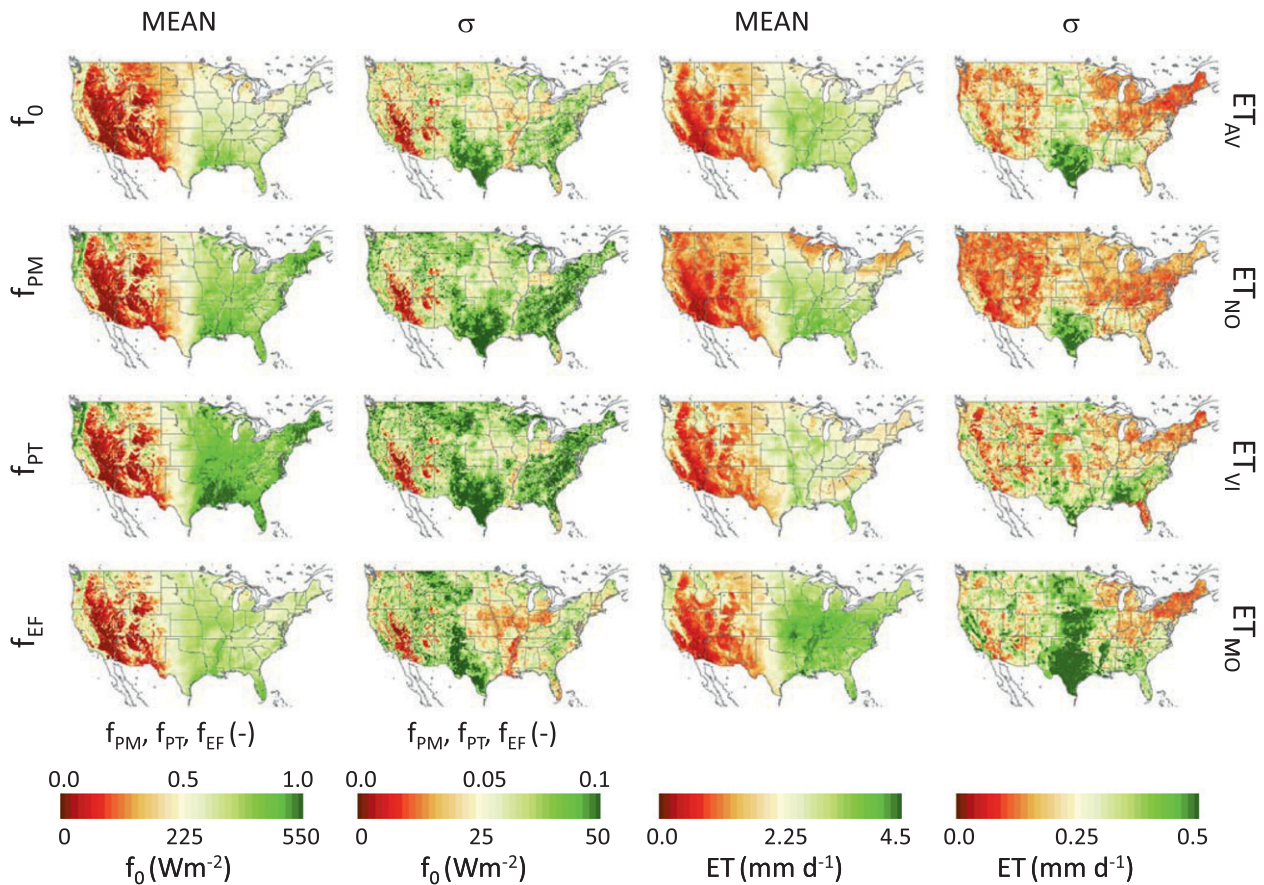


FIG. 4. (left two columns) Climatological mean and standard deviation maps for several ALEXI [ $f_0$  ( $W m^{-2}$ ) and  $f_{PM}$ ,  $f_{PT}$ , and  $f_{EF}$  (unitless)] and (right two columns) NLDAS ET-related indicators ( $mm d^{-1}$ ) included in the intercomparison, computed from 26-week (April–September) composites over the period 2000–11.

temporal correlations between monthly values of ESI and other drought indicators are plotted graphically in Fig. 6. Average monthly spatial correlations give almost identical rankings, but tend to be lower by 0.03 on average.

The statistical metrics in Fig. 6 give general information regarding relative index congruence. Among all indices included in the intercomparison, USDM anomalies were most highly correlated in both space and time, with SM anomalies at 1-month time scales from the NLDAS ensemble average ( $SM_{AV-1}$ ), with  $\langle r \rangle = 0.66$ . Of the individual NLDAS models, VIC SM anomalies provided best agreement with temporal and spatial patterns in USDM, followed by Noah, although differences were small. In comparison with the remote sensing indices (ESI, ETI, and VHI), the USDM was best correlated with ESI-3, with temporal  $\langle r \rangle = 0.55$ . USDM correlations with ETI and VHI are similar, with  $\langle r \rangle = 0.45$ – $0.48$ . Both outperform ET anomalies from NLDAS according to this metric, varying between  $\langle r \rangle = 0.33$ – $0.47$ . For most indices, with the exception of NLDAS

SM anomalies, agreement with USDM classification improves with increasing index compositing time scale, reflecting the conservative nature of USDM classifications over time.

The strongest correlations between ALEXI and NLDAS indicators listed in Fig. 6 are with NLDAS SM rather than ET, with maximum temporal  $\langle r \rangle = 0.69$  for ESI-3 and  $SM_{AV-2}$ . Normalization of ALEXI ET by reference ET and restriction to clear-sky conditions both serve to minimize impacts of radiation forcing that dominates variability in NLDAS daily (all sky) ET in many parts of the CONUS domain. In comparison with ESI, NLDAS SM correlations are lower with ETI, with  $\langle r \rangle = 0.58$  for ETI-3 and  $SM_{AV-2}$ , again indicating the value of the scaling flux in ESI for isolating surface moisture effects from radiation effects. Of the remote sensing indices, VHI consistently has the lowest correlations with precipitation-related indices. In comparison with ESI correlations, VHI correlations are lower on average by 0.05 with USDM, by 0.08 with NLDAS ET, and by 0.17 with NLDAS SM anomalies.

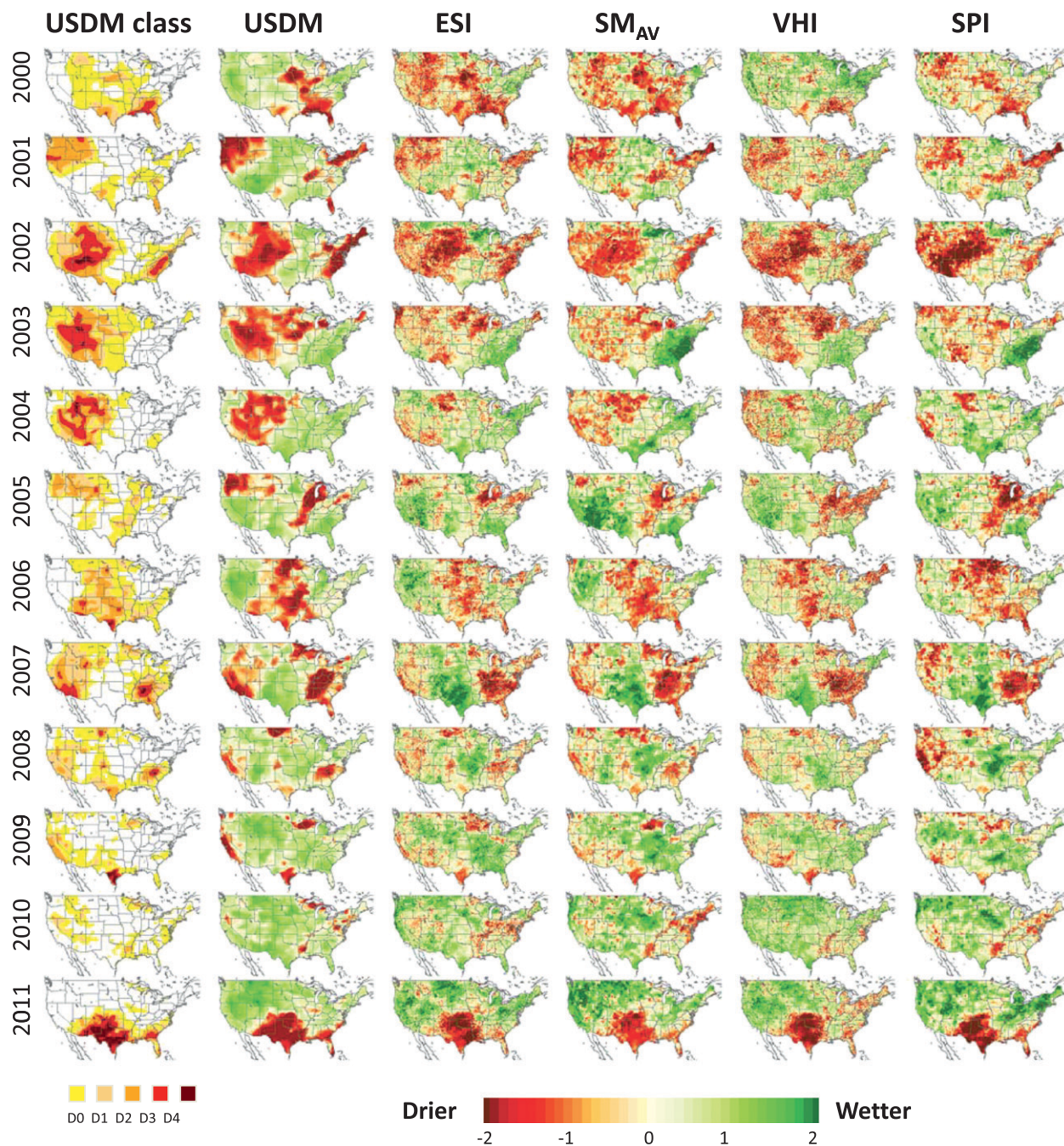


FIG. 5. Seasonal anomalies in 26-week composites of USDM, ESI,  $SM_{AV}$ , VHI, and SPI for 2000–11, along with average USDM class recorded for each year during the period April–September.

Further investigation reveals how interindex correlations vary spatially across CONUS. Figure 7 shows maps of temporal correlation coefficients computed between select remote sensing– and precipitation-based indices (3-month composites) and with anomalies in USDM drought classifications. Plots of correlations with output from individual NLDAS LSMs appear similar to those

with the ensemble averages, but with somewhat lower mean values (not shown).

In general, time series from index pairs are best correlated along a north–south band through the central United States. This region lies along a sharp east–west gradient in precipitation and vegetation cover, where the seasonal cycling and interannual variability in soil

		Remote sensing-based indicators									
		USDM	ESI-1	ESI-2	ESI-3	ETI-1	ETI-2	ETI-3	VHI-1	VHI-2	VHI-3
Precipitation-based indicators	USDM	-----	0.517	0.537	0.554	0.445	0.470	0.478	0.464	0.474	0.474
	ET <sub>MO</sub> -1	0.389	0.496	0.435	0.410	0.485	0.414	0.386	0.377	0.326	0.291
	ET <sub>MO</sub> -2	0.436	0.513	0.522	0.498	0.508	0.509	0.478	0.441	0.414	0.374
	ET <sub>MO</sub> -3	0.466	0.501	0.534	0.540	0.496	0.529	0.533	0.445	0.440	0.415
	ET <sub>NO</sub> -1	0.330	0.452	0.410	0.387	0.500	0.446	0.419	0.352	0.325	0.296
	ET <sub>NO</sub> -2	0.358	0.431	0.457	0.443	0.476	0.512	0.488	0.384	0.378	0.351
	ET <sub>NO</sub> -3	0.379	0.414	0.452	0.467	0.455	0.508	0.528	0.372	0.383	0.369
	ET <sub>VI</sub> -1	0.386	0.440	0.433	0.425	0.483	0.449	0.433	0.372	0.357	0.336
	ET <sub>VI</sub> -2	0.414	0.421	0.459	0.465	0.466	0.504	0.495	0.399	0.396	0.380
	ET <sub>VI</sub> -3	0.431	0.403	0.448	0.474	0.447	0.501	0.525	0.378	0.390	0.385
	ET <sub>AV</sub> -1	0.418	0.525	0.480	0.457	0.547	0.485	0.456	0.409	0.369	0.337
	ET <sub>AV</sub> -2	0.444	0.509	0.535	0.523	0.536	0.556	0.530	0.458	0.444	0.411
	ET <sub>AV</sub> -3	0.458	0.480	0.521	0.544	0.504	0.549	0.558	0.454	0.464	0.450
	SM <sub>MO</sub> -1	0.619	0.617	0.639	0.648	0.524	0.542	0.541	0.436	0.438	0.432
	SM <sub>MO</sub> -2	0.606	0.566	0.623	0.649	0.480	0.531	0.544	0.411	0.431	0.436
	SM <sub>MO</sub> -3	0.591	0.524	0.585	0.628	0.444	0.500	0.529	0.383	0.410	0.425
	SM <sub>NO</sub> -1	0.631	0.640	0.654	0.649	0.552	0.567	0.555	0.495	0.495	0.479
	SM <sub>NO</sub> -2	0.624	0.591	0.649	0.664	0.507	0.561	0.566	0.467	0.491	0.489
	SM <sub>NO</sub> -3	0.613	0.549	0.616	0.654	0.467	0.529	0.555	0.434	0.467	0.481
	SM <sub>VI</sub> -1	0.625	0.657	0.658	0.639	0.559	0.565	0.544	0.509	0.496	0.470
SM <sub>VI</sub> -2	0.630	0.615	0.669	0.673	0.522	0.573	0.571	0.492	0.510	0.499	
SM <sub>VI</sub> -3	0.628	0.576	0.643	0.675	0.485	0.547	0.570	0.462	0.494	0.504	
SM <sub>AV</sub> -1	0.657	0.669	0.683	0.677	0.570	0.584	0.572	0.500	0.497	0.480	
SM <sub>AV</sub> -2	0.651	0.617	0.677	0.693	0.523	0.578	0.584	0.475	0.496	0.494	
SM <sub>AV</sub> -3	0.638	0.569	0.637	0.678	0.479	0.542	0.570	0.442	0.475	0.487	
SPI-3	0.484	0.554	0.551	0.529	0.489	0.492	0.467	0.424	0.404	0.371	
SPI-6	0.577	0.535	0.562	0.580	0.470	0.501	0.515	0.428	0.439	0.440	
SRI-3	0.489	0.475	0.511	0.529	0.390	0.421	0.431	0.323	0.334	0.335	
SRI-6	0.503	0.431	0.480	0.516	0.365	0.407	0.431	0.301	0.318	0.331	

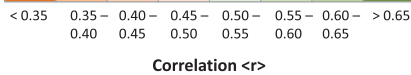


FIG. 6. Average temporal correlation coefficient,  $\langle r \rangle$ , computed between remote sensing drought indicators (columns) and precipitation-based indices (rows) for April–October of 2000–11.

moisture availability is strongest and ET is largely soil-moisture limited, enhancing correlations between SM and ET. This band across the Great Plains has been identified in global simulations as a region of exceptionally strong land–atmosphere coupling during the boreal summer, along with the Sahel in North Africa and the Indus Valley (Koster et al. 2004, 2006; Dirmeyer 2011). The VHI shows a tendency for lower or negative correlation with all precipitation indices at higher latitudes, particularly in the northeast. This is in agreement with findings by Karnieli et al. (2010), who demonstrated that under conditions of energy-limited vegetation growth (high latitudes and elevations and during the winter/early spring), temperature and vegetation cover can be positively correlated, yielding a false signal in VHI that assumes a negative correlation. NLDAS ET<sub>AV</sub> is also anticorrelated with USDM in parts of the northern United States, including northeastern Minnesota, the upper peninsula of Michigan, and Washington. This may be due in part to cloud cover contributions, which reduce all-sky ET during rainier/wetter periods. ETI, based on clear-sky flux, does not show these strong anticorrelation features and yields higher average correlation than either VHI or ET<sub>AV</sub>. Normalization with the PM scaling flux

(i.e., ESI) further improves correlation with USDM and SM over all parts of the geographic domain. Spatial patterns in temporal correlation between ESI and NLDAS SM anomalies across CONUS evident in Fig. 7 are similar to those identified by Hain et al. (2011), who investigated joint assimilation of TIR (ALEXI ET/ $F_{ref}$ ) and microwave soil moisture information into the Noah model.

Figure 8 shows differences in index temporal correlation with USDM and SM<sub>AV</sub>-3, identifying regions where differences were statistically significant at  $p < 0.05$  according to Fisher’s  $z$  transformation test with degrees of freedom adjusted for temporal autocorrelation. Correlation differences were computed as  $r(\text{ESI-3}) - r(x)$ , where  $r(\text{ESI-3})$  is the temporal correlation between ESI-3 and USDM or SM<sub>AV</sub>-3, and  $r(x)$  is the correlation between index  $x$  and USDM or SM<sub>AV</sub>-3. Green tones indicate areas where  $r(\text{ESI-3}) > r(x)$ . Over most of the domain, SM<sub>AV</sub> was a better indicator of USDM drought class during this time period than was ESI, particularly in the western United States, where ET is climatologically low and the ET/ $F_{ref}$  signal is small (upper left panel). This is not unexpected. Both NLDAS SM anomalies and USDM drought classifications primarily reflect deficits in precipitation observations, and thus, there is some level of inherent interdependence between these indicators. Furthermore, NCEP–NLDAS indices have been used to some extent in the construction of the USDM since 2010. In contrast, the ESI is developed without precipitation data and was not used in the USDM classification process during the time period covered by this study and can be considered an independent index.

The ETI-3 panels in Fig. 8 (second row) demonstrate that the value of including the PM scaling flux is most notable (in terms of increased correlation with USDM and NLDAS SM) in the lower Mississippi River basin. In comparison with ESI-3, ET from NLDAS (ET<sub>AV</sub>-3) is the most decoupled from NLDAS SM in the northeastern United States, where evaporative fluxes are typically radiation limited rather than moisture limited (third row). This same region is highlighted in the correlation differences with VHI-3, indicating decreased skill in VHI at reflecting SM conditions in the northeast (fourth row). In contrast, in comparison with SPI-3, ESI-3 adds value in the western United States, where evaporative losses (not captured in the SPI) are a major driver of SM dynamics (bottom row).

#### 4) MONTHLY SPATIAL CORRELATIONS

Figure 9 demonstrates the time variability in spatial correlations computed between select index pairs sampled at monthly intervals. All plots exhibit annual seasonality, with lower spatial correlations typically observed during the winter months. Certain years with strong

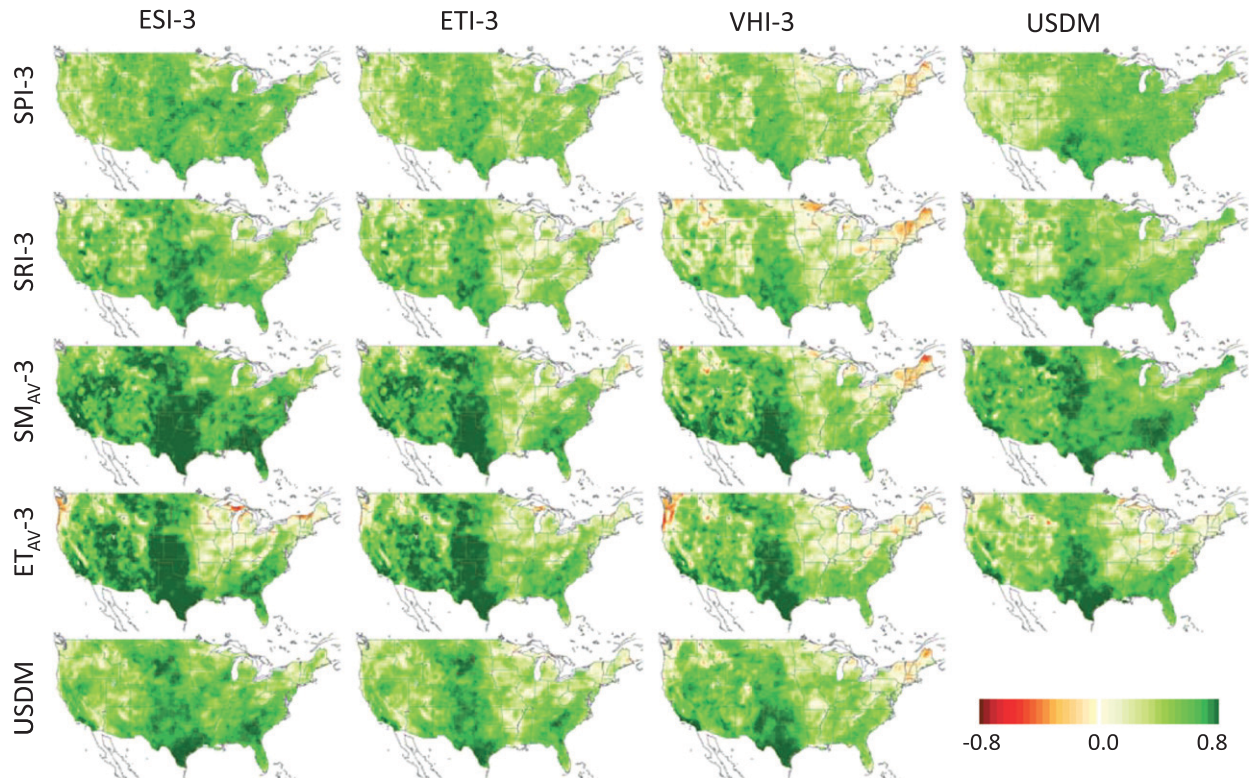


FIG. 7. Maps of temporal correlation coefficient computed between time series of select remote sensing (ESI, ETI, and VHI on horizontal axis) and precipitation-based indices (SPI, SRI,  $SM_{AV}$ , and  $ET_{AV}$  on vertical axis) at 3-month time scales, and with anomalies in USDM drought classifications.

spatial drought patterns have consistently higher correlations among indices, in particular, 2002/03, 2007, and 2011 (see Fig. 5).

In this comparison, USDM (top row) shows the strongest spatial and most temporally consistent correlations with  $SM_{AV}$  anomalies, followed by the runoff index computed from the NLDAS ensemble. Of the remote sensing indices, ESI is most strongly correlated with USDM over this time period, outperforming both ETI and VHI.  $ET_{AV}$ , VHI, and SPI show the largest degradation in spatial consistency with other indicators during the winter months.

SM anomalies (middle row) are highly correlated with SRI, which may be expected because both are generated by NLDAS LSMs based on physical relationships assumed between soil moisture and runoff. This ranking holds for other time scales as well. Of the remote sensing indices, SM is spatially best correlated with ESI. During the growing season, SM anomaly patterns are more similar to ESI than to USDM classes, but the correlation with ESI weakens during the winter seasons when the ET signal is low. Correlations between SM anomalies and VHI are consistently lower than with ESI.

In comparison with the precipitation indices, ESI (bottom row) shows stronger correlations with SM

anomalies and SRI than with SPI, indicating a closer relationship of  $ET/F_{ref}$  with storage and runoff components of the hydrologic budget than with water supply (precipitation). Seasonal cycles in spatial consistency between ESI and ETI reflect the impact of the scaling flux, with highest correlations midseason when the slope of ET time curve is close to zero (Fig. 3), and both ESI and ETI sample similar anomalies.

In summary, NLDAS SM anomalies appear to be the best predictor of patterns in USDM drought class, while ESI shows best performance of the remote sensing indices tested. Despite the simplicity of its formulation and data demands, the VHI also performed reasonably well during much of the growing season, except under conditions of energy-limited vegetation growth.

### c. Analyses of drought events

Time series of ESI and SM anomalies extracted at several sites across CONUS (Fig. 2) are displayed in Fig. 10 to demonstrate response to major regional drought events over the past 12 years. Also indicated are the associated USDM anomalies and drought classes at these sites. All data have been averaged over  $50\text{ km} \times 50\text{ km}$  boxes, sampling paired sites covering a range of climatic conditions and land use. SM anomalies from each of the three

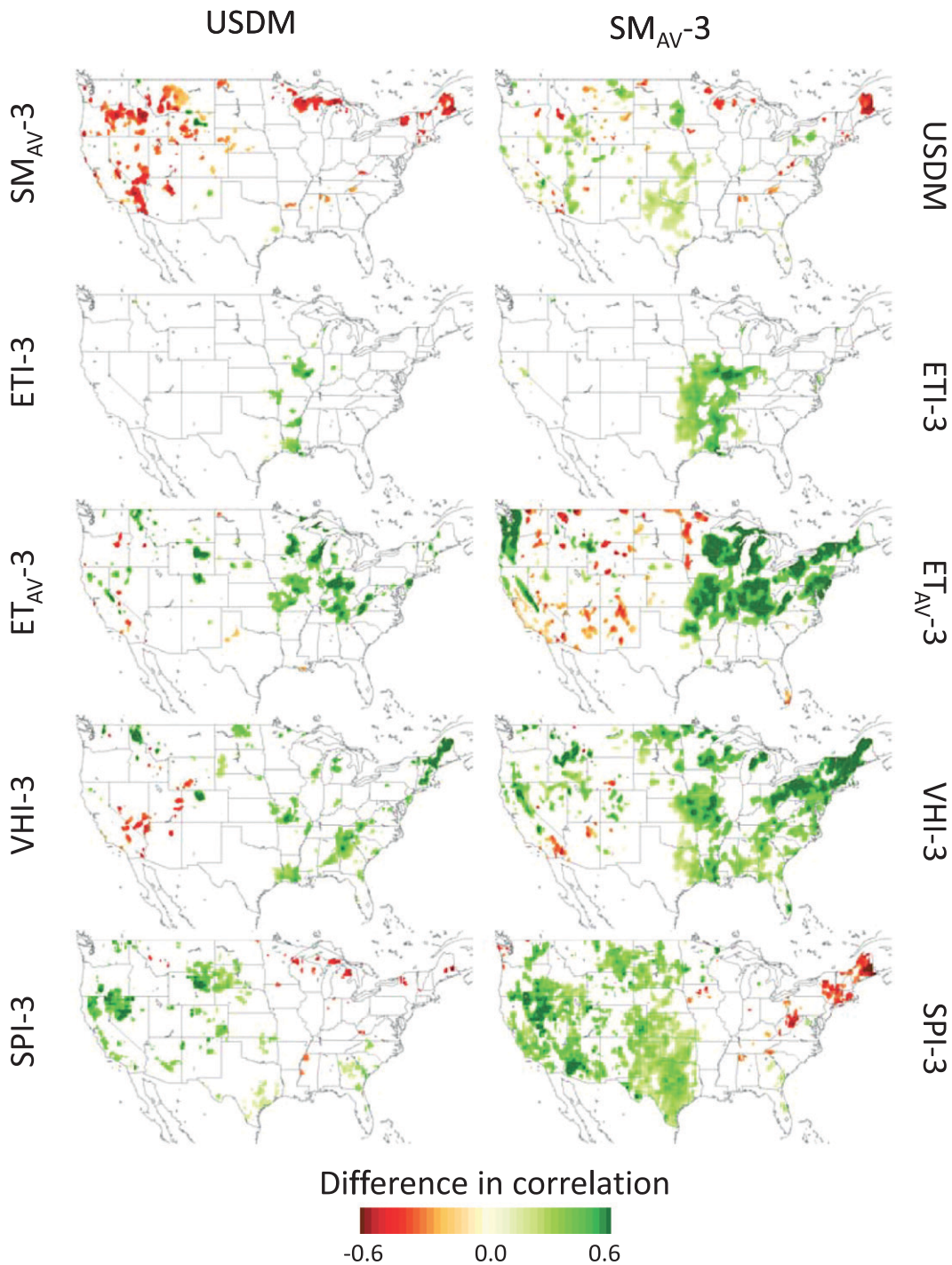


FIG. 8. Difference in interindex temporal correlation computed as  $r(\text{ESI-3}) - r(x)$ , where  $r(\text{ESI-3})$  is the temporal correlation between ESI-3 and (left) USDM or (right)  $\text{SM}_{\text{AV-3}}$  and  $r(x)$  is the correlation between index  $x$  and USDM or  $\text{SM}_{\text{AV-3}}$ . Comparison indices  $x$  include (second row) ETI-3, (third row)  $\text{ET}_{\text{AV-3}}$ , (fourth row) VHI-3, and (bottom row) SPI-3. Green shading indicates  $r(\text{ESI-3}) > r(x)$ . Only pixels with significant ( $p < 0.05$ ) correlation differences are displayed.

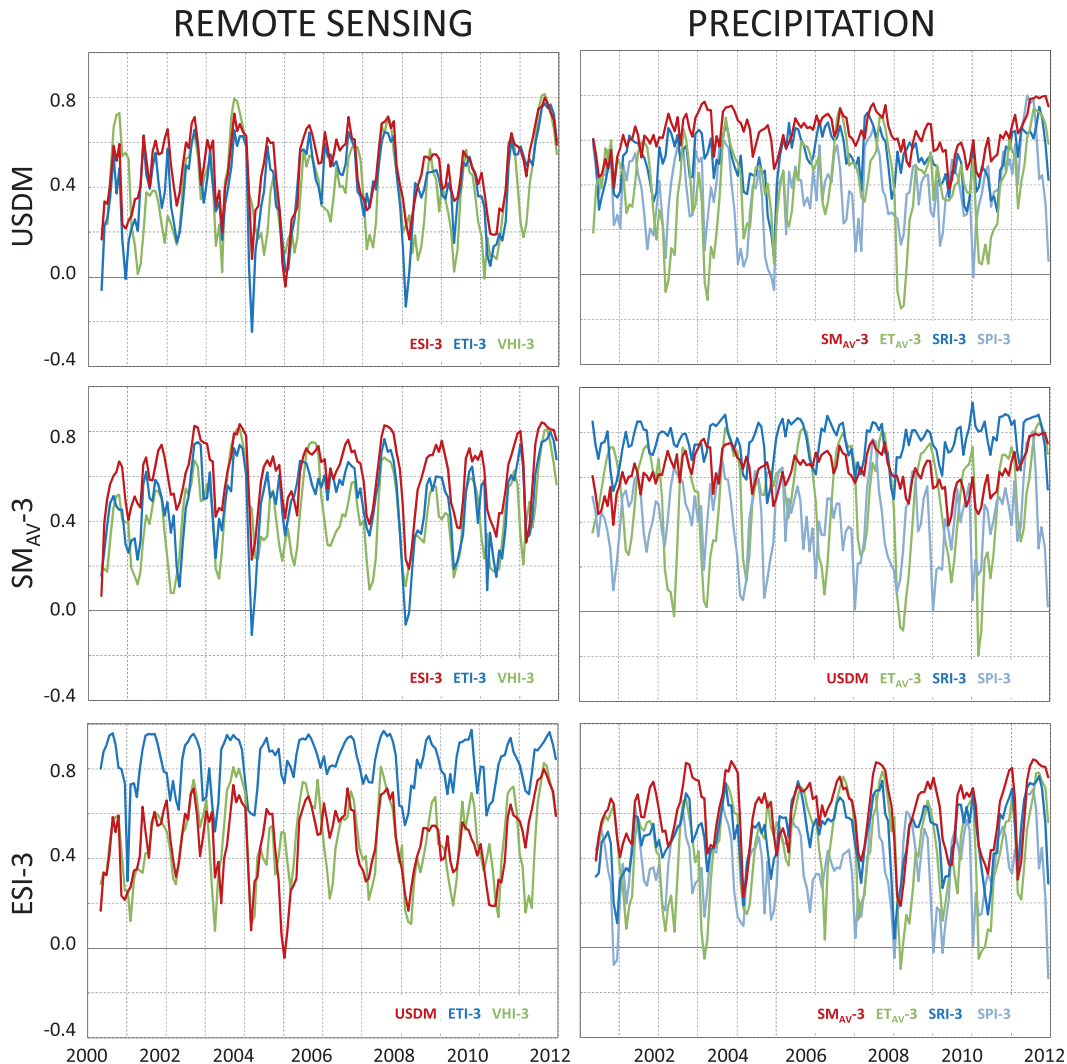


FIG. 9. Time series of spatial correlation coefficients computed between drought index pairs sampled at monthly intervals.

NLDAS models are shown to indicate variability within the ensemble.

Two points along the East Coast, in Georgia (GA) and North Carolina (NC), show reasonable temporal correspondence between indices, capturing the eastern droughts of 2002 and 2007 evident in Fig. 5. All indices track well, with relatively small spread among SM anomalies from the NLDAS models. The ensemble-averaged SM (not shown) provides best agreement with both ESI and USDM anomalies at most sites.

Even tighter agreement between SM anomalies, and with ESI, is observed at two points in south Texas (TX) and western Oklahoma (OK). Correlations with the USDM are strong in this part of the United States, which was characterized by low vegetation cover and strong moisture variability over the past decade. Both points

exhibit drought impacts in 2006 and 2011, while the Texas drought of 2009 did not extend into the central plains. In 2000, the ESI captures impacts of a flash drought that occurred over Oklahoma and is missed by the SM indices in the sampled area. This event is further explored in section 4d.

Time traces from two points in Iowa (IA-N and IA-S, also sampled in Fig. 3) demonstrate variable ESI performance over the Corn Belt. At both sites, the ESI shows stronger month-to-month variability than do the NLDAS SM anomalies. Still, the correlation with SM and USDM is reasonable at longer time scales at the southern Iowa site, which has lower density of planted corn and soybean acreage. At this site, the Mosaic SM anomalies deviate significantly from the other LSMs, showing much lower temporal variability. At the northern Iowa site, in the

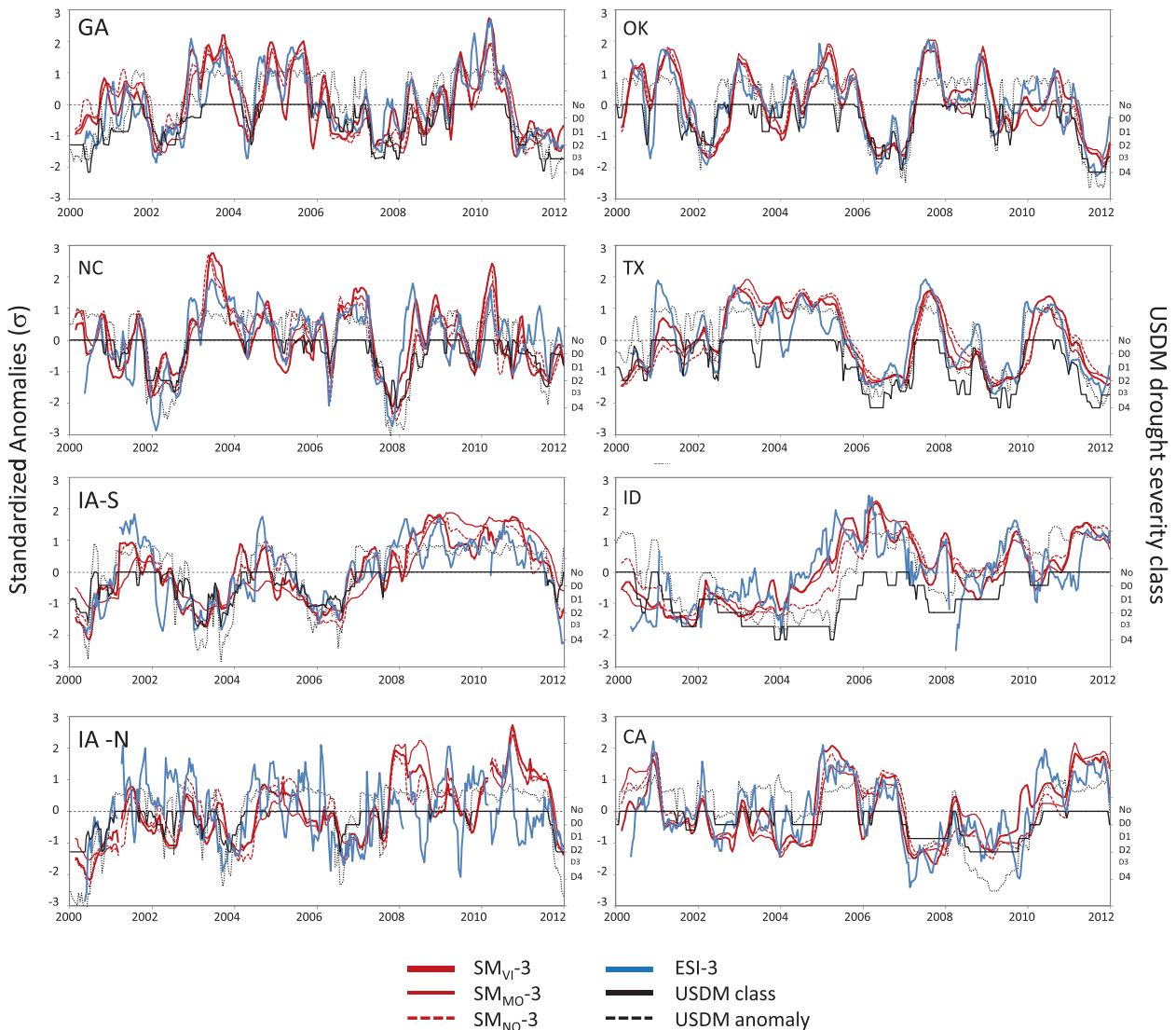


FIG. 10. Time series of ESI-3; anomalies in  $SM_{NO-3}$ ,  $SM_{MO-3}$ , and  $SM_{VI-3}$ ; and USDM drought classes and anomaly values for several sites across CONUS (Fig. 2), averaged over  $50 \text{ km} \times 50 \text{ km}$  boxes. In each panel, standardized anomalies are associated with the left vertical axis (in units of  $\sigma$ ), and USDM class with the right vertical axis.

heart of the Corn Belt, ESI is very noisy, although it still detects broad features in the interannual moisture signal. Because of the peaked nature of the annual curve (Fig. 3) in this part of the landscape, where the vegetation cycle is intensively managed,  $f_{PM}$  anomalies are likely dominated by effects of variable planting date, emergence, and crop growth rate, which may or may not be related to soil moisture conditions. Information content in this core part of the Corn Belt might be improved with phenology-based timing adjustments to the normal curves used in the anomaly computations. The SM variables from the various NLDAS models also show considerable spread in this region.

Finally, two areas supporting irrigated agriculture in the western United States are also plotted in Fig. 10: in the Snake River Plain in Idaho (ID) and the Central Valley of California (CA). Both regions exhibit effects of the long-term western drought of 2000–04, which is more pronounced in Idaho. In this region, divergence of SM and ESI time traces from USDM anomalies starting in 2003 show SM conditions improving while hydrologic drought classifications persisted in the USDM. This is not an error in the drought indicators, but a factor of temporal scale mismatch. In addition, USDM classifications also include impacts reported via the Drought Impact Reporter and through field input. This is an example of when simple correlations between indicators



FIG. 11. Time series of  $f_{PM}$  for sites in Fig. 10 that are not shown in Fig. 3.

do not tell the full story. Comparing  $f_{PM}$  curves at these sites (Fig. 11) to those at the Iowa sites (Fig. 3) demonstrates why ESI is better behaved in the Central Valley than in core of the Corn Belt. The longer growing season in California leads to less peaked seasonal water consumption. Higher variability in  $f_{PM}$  is noted during the winter growing season (day of year 0–130) than during the summer at the Central Valley site, but still there is good separation between  $f_{PM}$  curves because of variable moisture conditions, resulting in a strong wintertime ESI signal.

#### d. Monthly patterns and change detection

The efficacy of the ESI change product ( $\Delta ESI$ ) in identifying changes in historical USDM drought classifications is examined in Fig. 12. Monthly analyses are presented for 4 years with rapidly evolving drought conditions, including seasons showing signals of flash drought occurrence in 2000, 2001, 2003, and 2011. These figures also show monthly anomalies and first-order changes in the ensemble-averaged NLDAS SM products for comparison. ESI and SM change products are both displayed

as standardized anomalies, representing changes occurring over a 4-week interval. USDM changes ( $\Delta USDM$ ) are simple differences in drought class over the same 4-week period. Overlaid on  $\Delta USDM$  are contours highlighting generalized areas where both ESI and SM changes are strong ( $>1.5\sigma$ ), signaling areas of potential interest to drought monitors.

#### 1) 2000

Monthly patterns in ESI and  $SM_{AV}$  show strong similarity over the 2000 growing season (Fig. 12a). Both ESI and  $SM_{AV}$  indicated lower SM conditions in the western United States in April–June, well before a D0–D1 classification appears in the USDM in August. Signals of the western drought appeared in SPI-3 in May, but VHI does not significantly capture this event at any time during 2000 (not shown).

In May–July, both  $\Delta ESI$  and  $\Delta SM$  capture the primary hotspots of USDM class change. Use of the term “flash drought” was first applied to events in August and September of 2000, when an intense heat wave, windy conditions, and resulting high ET rates rapidly depleted

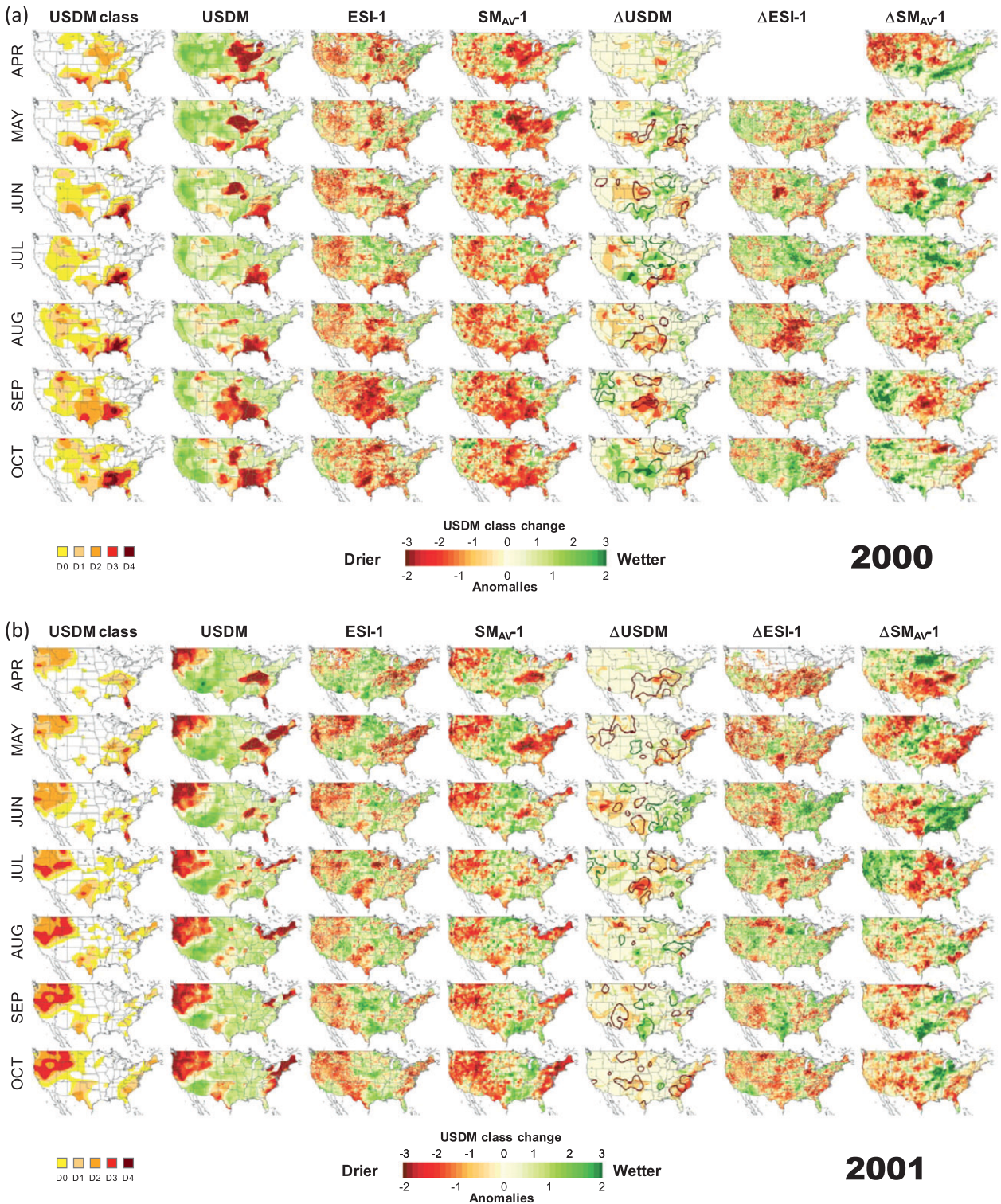


FIG. 12. (a)–(d) Monthly standardized anomalies in the USDM drought classes (USDM), 1-month ESI composites (ESI-1), 1-month ensemble-averaged SM anomalies ( $SM_{AV-1}$ ), as well as (first column) USDM drought classes for the week closest to the end of each month. Also shown are change indices  $\Delta ESI-1$ ,  $\Delta SM_{AV-1}$ , and  $\Delta USDM$  reflecting changes observed over 4-week intervals. Overlaid on  $\Delta USDM$  are contours indicating generalized areas where both  $\Delta ESI-1$  and  $\Delta SM_{AV-1}$  indicate large decreases (red shades) and increases (green shades) in surface moisture. Maps are shown for (a) 2000, (b) 2001, (c) 2003, and (d) 2011.

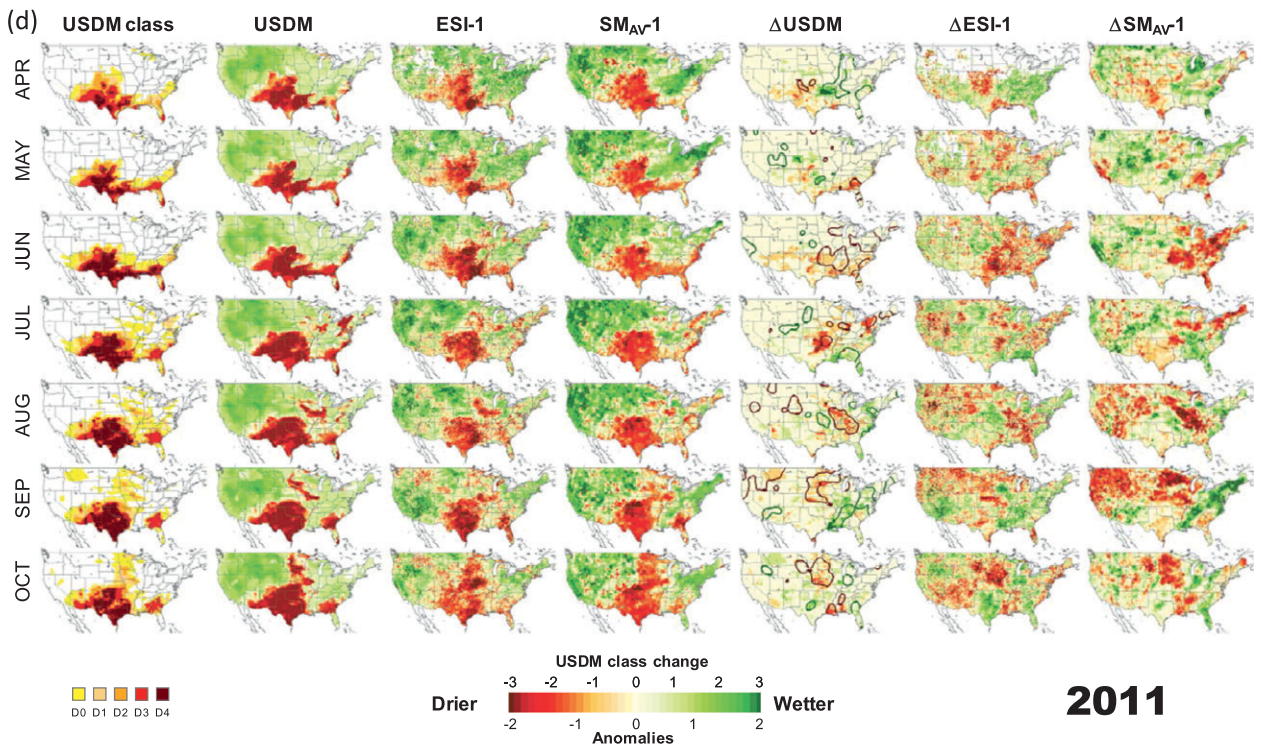
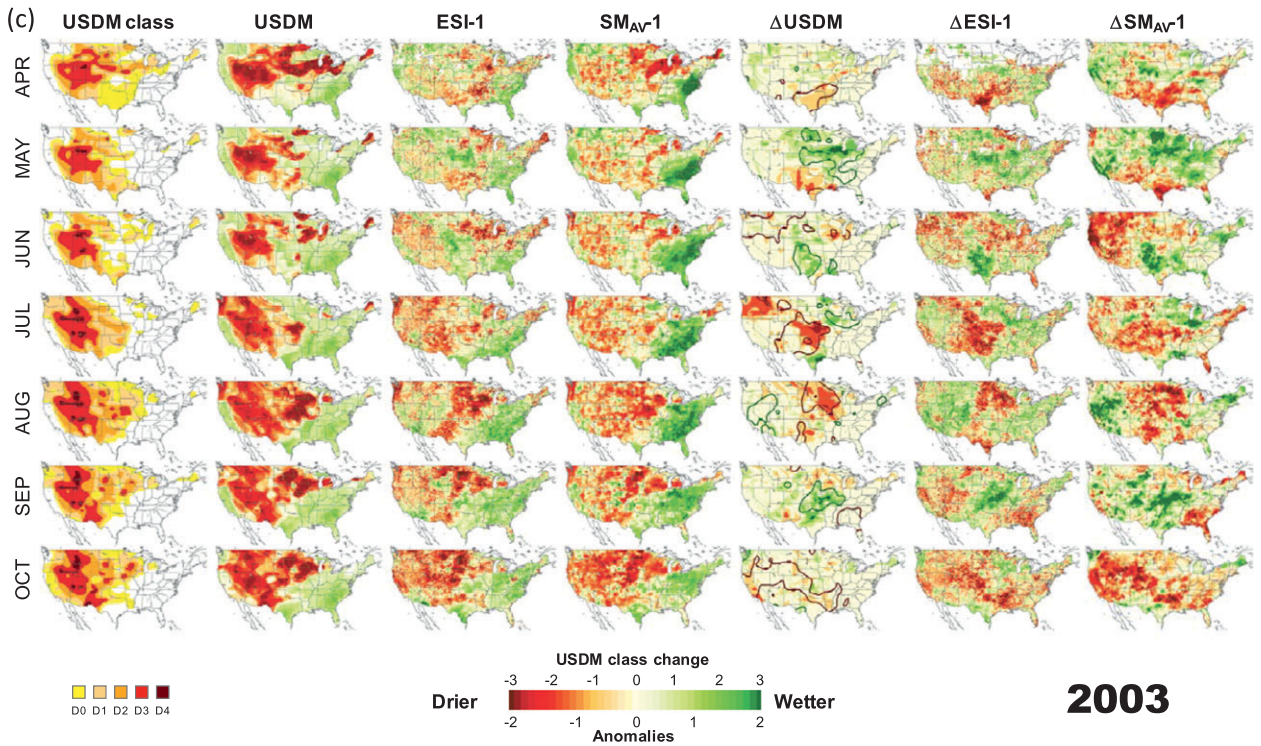


FIG. 12. (Continued)

available soil moisture in Oklahoma and Texas (M. Svoboda 2000, unpublished manuscript). This led to an abrupt transition between D0 and D2 drought severity class occurring in early September, associated with observed impacts on range and crop conditions, and an increase in wildfire activity. In July, the ESI indicated above-normal ET over the affected area as soil moisture reserves were being depleted. Signals of stress and moisture deficiency over this region were apparent first in  $\Delta$ ESI in the July-to-August change product, and somewhat later in  $\Delta$ SM. Note that early detection of moisture status changes may serve to decorrelate ESI and USDM signals; thus, future analyses will include variable lag times.

## 2) 2001

USDM, ESI, and  $SM_{AV}$  show similar patterns of drought evolution in 2001, with persistent dry conditions in the northwest and northeast (Fig. 12b). The most significant change event occurred between June and July, when D1 and D2 conditions rapidly spread from west Texas into Oklahoma. This was driven by intense heat coupled with below-average rainfall set up by a stationary ridge of high pressure, which caused crop and pasture conditions to significantly deteriorate by mid-July. Rainfall and cooler temperatures reduced the severity of drought in this region from late August to early September. These major changes, into and out of drought over Texas and Oklahoma, are clearly highlighted in the change products for July and September. During October,  $\Delta$ ESI and  $\Delta$  $SM_{AV}$  patterns agree well, but are less related to USDM changes, suggesting the normalized change signal may be less helpful near the very end of the growing season.

## 3) 2003

In April–August 2003,  $\Delta$ ESI was effective in isolating regions of strong drought class change (Fig. 12c). The D1 drought over the northwest in July was signaled a month earlier by  $\Delta$ ESI and  $\Delta$  $SM_{AV}$ . Rapid expansion of drought conditions over the central United States in July due to a prolonged heat wave left vegetation stressed and moisture deprived. D1 drought conditions pushed into Minnesota and Wisconsin in August. These rapid changes are quite evident in all change indicators, but are better localized in  $\Delta$ ESI than  $\Delta$  $SM_{AV}$ . While these changes can also be seen in the ESI itself, the change product shows added utility in focusing attention on regions of particular timely interest.

## 4) 2011

The severe Texas drought of 2011 is captured with good spatial detail by both ESI and  $SM_{AV}$  (Fig. 12d).

Besides this area of persistent drought, which does not factor strongly into the change products, another rapid onset or flash drought event occurred in 2011, beginning in June over Arkansas and spreading to Missouri and states to the north in July. While precipitation deficits were observed, they were not extreme. Rather, the spread of drought was fueled by strong winds and high temperatures that lead to higher ET demands and rapid depletion of soil moisture conditions. Advance warning of this expansion was indicated in  $\Delta$ ESI and  $\Delta$  $SM_{AV}$  from May to June and may have allowed for an earlier response. Routine generation of drought index change products, such as those shown in Fig. 12, could benefit state-of-the-art USDM classifications by allowing earlier identification of emerging areas of interest.

## 5. Conclusions

In this study, a suite of TIR-based remote sensing drought indicators were compared with SM, ET, and runoff anomalies generated using the NCEP NLDAS modeling system and historic USDM drought severity classifications converted into anomaly form. The purpose of the study was to 1) optimize the ESI format with respect to SM and USDM anomalies, 2) establish the performance of this new remote sensing index relative to existing NLDAS indices, 3) investigate similarity between indices in terms of spatiotemporal patterns and first-order changes; and 4) motivate the value of a derived change product as a potential drought early warning tool.

Results demonstrate that a scaling flux adds value to ET anomalies, serving to reduce impact of seasonality and nonprecipitation-related ET drivers and better reflect moisture variability. A scaling flux based on the Penman–Monteith equation for potential ET provided the best agreement with other drought indicators. Temporal smoothing of scaled flux time series further improved agreement, reducing noise due to incomplete cloud clearing in the ET remote sensing retrievals.

In comparison with prior USDM classifications for 2000–11, anomalies in NLDAS ensemble-averaged SM agreed best of the drought indicators evaluated here. SM anomalies were more closely related to USDM classes than was SPI, suggesting that interpretive value is added by processing precipitation data through an LSM. Of the remote sensing indices evaluated, ESI was best correlated with NLDAS indices and with USDM classes. Both ESI and related remote sensing ET index ETI (ESI with no scaling flux) outperformed anomalies in NLDAS daily ET (all sky). This may be in part because of the focus on clear-sky fluxes in ETI and ESI, isolating impacts of clouds on ET from those of surface moisture. The VHI showed anticorrelation with USDM and NLDAS SM in

spring/winter at high latitudes, but functioned reasonably well in many cases given the simplicity of the index formulation.

Further comparison of spatial and temporal patterns in ESI, NLDAS SM, and USDM revealed good agreement over much of CONUS, particularly in the central United States, where there was strong year-to-year variability in moisture conditions. Parts of the central Corn Belt, in northern Iowa and southern Minnesota, show strongly peaked seasonal variability in  $ET/F_{ref}$  for all ESI scaling fluxes tested. This results in reduced correlations with ESI, because anomalies with respect to fixed normal conditions reflect both moisture and crop phenology differences between years (e.g., delays in planting and emergence mimic moisture reductions in ET). Future work will focus on implementing normals indexed by phenological stage (e.g., days since emergence) rather than calendar year over highly managed parts of the monitoring domain.

Both ESI and NLDAS SM change products indicated value in providing early warning of changing drought conditions recorded in the USDM. A convergence of evidence approach applied to independently derived change indicators may prove useful in assessing the validity of rapidly evolving drought conditions. Further research is in progress to address optimal methods for merging prognostic and diagnostic drought and change signals and to develop thresholds and visualization methods that clearly and reliably identify rapid-onset drought occurrence.

*Acknowledgments.* This work was supported by NOAA/CTB Grant GC09-236 and by Vaadia-BARD Postdoctoral Fellowship Award No. FI-421-2009 from BARD, the United States–Israel Binational Agricultural Research and Development Fund.

#### REFERENCES

- Allen, R. G., L. S. Pereira, D. Raes, and M. Smith, 1998: Crop Evapotranspiration: Guidelines for computing crop water requirements. FAO Irrigation and Drainage Paper 56, 300 pp. [Available online at <http://www.fao.org/docrep/X0490E/X0490E00.htm>.]
- , M. Tasumi, and R. Trezza, 2007: Satellite-based energy balance for mapping evapotranspiration with internalized calibration (METRIC)—Model. *J. Irrig. Drain. Eng.*, **133**, 380–394, doi:10.1061/(ASCE)0733-9437(2007)133:4(380).
- Anderson, M. C., J. M. Norman, G. R. Diak, W. P. Kustas, and J. R. Mecikalski, 1997: A two-source time-integrated model for estimating surface fluxes using thermal infrared remote sensing. *Remote Sens. Environ.*, **60**, 195–216.
- , —, J. R. Mecikalski, J. A. Otkin, and W. P. Kustas, 2007a: A climatological study of evapotranspiration and moisture stress across the continental U.S. based on thermal remote sensing: 1. Model formulation. *J. Geophys. Res.*, **112**, D10117, doi:10.1029/2006JD007506.
- , —, —, —, and —, 2007b: A climatological study of evapotranspiration and moisture stress across the continental U.S. based on thermal remote sensing: 2. Surface moisture climatology. *J. Geophys. Res.*, **112**, D11112, doi:10.1029/2006JD007507.
- , C. R. Hain, B. Wardlow, J. R. Mecikalski, and W. P. Kustas, 2011: Evaluation of a drought index based on thermal remote sensing of evapotranspiration over the continental United States. *J. Climate*, **24**, 2025–2044.
- , and Coauthors, 2012: Mapping daily evapotranspiration at Landsat spatial scales during the BEAREX'08 field campaign. *Adv. Water Resour.*, **50**, 162–177.
- Barlage, M., and Coauthors, 2010: Noah land surface model modifications to improve snowpack prediction in the Colorado Rocky Mountains. *J. Geophys. Res.*, **115**, D22101, doi:10.1029/2009JD013470.
- Betts, A. K., F. Chen, K. E. Mitchell, and Z. I. Janjic, 1997: Assessment of the land surface and boundary layer models in two operational versions of the NCEP Eta model using FIFE data. *Mon. Wea. Rev.*, **125**, 2896–2916.
- Bowling, L. C., and D. P. Lettenmaier, 2010: Modeling the effects of lakes and wetlands on the water balance of Arctic environments. *J. Hydrometeorol.*, **11**, 276–295.
- Brown, J. F., B. D. Wardlow, T. Tadesse, M. J. Hayes, and B. C. Reed, 2008: The Vegetation Drought Response Index (VegDRI): A new integrated approach for monitoring drought stress in vegetation. *GISci. Remote Sens.*, **45**, 16–46.
- Burnash, R. J. C., 1995: The NWS river forecast system—Catchment modeling. *Computer Models of Watershed Hydrology*, V. P. Singh, Ed., Water Resources Publications, 311–366.
- Daly, C., R. P. Neilson, and D. L. Phillips, 1994: A statistical-topographic model for mapping climatological precipitation over mountainous terrain. *J. Appl. Meteor.*, **33**, 140–158.
- Delogu, E., and Coauthors, 2012: Reconstruction of temporal variations of evapotranspiration using instantaneous estimates at the time of satellite overpass. *Hydrol. Earth Syst. Sci.*, **16**, 2995–3010.
- Dirmeyer, P. A., 2011: The terrestrial segment of soil moisture–climate coupling. *Geophys. Res. Lett.*, **38**, L16702, doi:10.1029/2011GL048268.
- , X. Gao, M. Zhao, Z. Guo, T. Oki, and N. Hanasaki, 2006: GSWP-2: Multimodel analysis and implications for our perception of the land surface. *Bull. Amer. Meteor. Soc.*, **87**, 1381–1397.
- Ek, M. B., K. E. Mitchell, Y. Lin, E. Rogers, P. Grunmann, V. Koren, G. Gayno, and J. D. Tarpley, 2003: Implementation of Noah land surface model advances in the National Centers for Environmental Prediction operational mesoscale Eta model. *J. Geophys. Res.*, **108**, 8851, doi:10.1029/2002JD003296.
- Fan, Y., and H. van den Dool, 2004: Climate Prediction Center global monthly soil moisture data set at 0.5° resolution for 1948 to present. *J. Geophys. Res.*, **109**, D10102, doi:10.1029/2003JD004345.
- Hain, C. R., W. T. Crow, J. R. Mecikalski, M. C. Anderson, and T. Holmes, 2011: An intercomparison of available soil moisture estimates from thermal infrared and passive microwave remote sensing and land surface modeling. *J. Geophys. Res.*, **116**, D15107, doi:10.1029/2011JD015633.
- , —, M. C. Anderson, and J. R. Mecikalski, 2012: An ensemble Kalman filter dual assimilation of thermal infrared and microwave satellite observations of soil moisture into the

- Noah land surface model. *Water Resour. Res.*, **48**, W11517, doi:10.1029/2011WR011268.
- Hayes, M., M. Svoboda, N. Wall, and M. Widhalm, 2011: The Lincoln Declaration on drought indices: Universal meteorological drought index recommended. *Bull. Amer. Meteor. Soc.*, **92**, 485–488.
- Houborg, R., M. Rodell, B. Li, R. H. Reichle, and B. F. Zaitchik, 2012: Drought indicators based on model-assimilated Gravity Recovery and Climate Experiment (GRACE) terrestrial water storage observation. *Water Resour. Res.*, **48**, W07525, doi:10.1029/2011WR011291.
- Karnieli, A., N. Agam, R. T. Pinker, M. C. Anderson, M. L. Imhoff, G. G. Gutman, N. Panov, and A. Goldberg, 2010: Use of NDVI and land surface temperature for drought assessment: Merits and limitations. *J. Climate*, **23**, 618–633.
- Knapp, K. R., 2008: Scientific data stewardship of International Satellite Cloud Climatology Project B1 geostationary observations. *J. Appl. Remote Sens.*, **2**, 023548, doi:10.1117/1.3043461.
- Kogan, F. N., 1995: Application of vegetation index and brightness temperature for drought detection. *Adv. Space Res.*, **15**, 91–100.
- , 1997: Global drought watch from space. *Bull. Amer. Meteor. Soc.*, **78**, 621–636.
- Koster, R. D., and M. J. Suarez, 1994: The components of a SVAT scheme and their effects on a GCM's hydrological cycle. *Adv. Water Resour.*, **17**, 61–78.
- , and —, 1996: Energy and water balance calculations in the Mosaic LSM. Technical Report Series on Global Modeling and Data Assimilation, NASA Tech. Memo 104606, Vol. 9, 66 pp. [Available online at <http://gmao.gsfc.nasa.gov/pubs/docs/Koster130.pdf>.]
- , —, and M. Heiser, 2000: Variance and predictability of precipitation at seasonal-to-interannual timescales. *J. Hydrometeorol.*, **1**, 26–46.
- , and Coauthors, 2004: Regions of strong coupling between soil moisture and precipitation. *Science*, **305**, 1138–1140.
- , and Coauthors, 2006: GLACE: The Global Land–Atmosphere Coupling Experiment. Part I: Overview. *J. Hydrometeorol.*, **7**, 590–610.
- Liang, X., D. P. Lettenmaier, E. F. Wood, and S. J. Burges, 1994: A simple hydrologically based model of land surface water and energy fluxes for GSMs. *J. Geophys. Res.*, **99**, 14415–14428.
- , E. F. Wood, and D. P. Lettenmaier, 1996: Surface and soil moisture parameterization of the VIC-2L model: Evaluation and modifications. *Global Planet. Change*, **13**, 195–206.
- Livneh, B., Y. Xia, K. E. Mitchell, M. B. Ek, and D. P. Lettenmaier, 2010: Noah LSM snow model diagnostics and enhancements. *J. Hydrometeorol.*, **11**, 721–738.
- McKee, T. B., N. J. Doesken, and J. Kleist, 1993: The relationship of drought frequency and duration to time scales. Preprints, *Eighth Conf. on Applied Climatology*, Anaheim, CA, Amer. Meteor. Soc., 179–184.
- , —, and —, 1995: Drought monitoring with multiple time scales. Preprints, *Ninth Conf. on Applied Climatology*, Dallas, TX, Amer. Meteor. Soc., 233–236.
- Mecikalski, J. M., G. R. Diak, M. C. Anderson, and J. M. Norman, 1999: Estimating fluxes on continental scales using remotely sensed data in an atmosphere–land exchange model. *J. Appl. Meteor.*, **38**, 1352–1369.
- Mesinger, F., and Coauthors, 2006: North American Regional Reanalysis. *Bull. Amer. Meteor. Soc.*, **87**, 343–360.
- Mitchell, K. E., and Coauthors, 2004: The multi-institution North American Land Data Assimilation System (NLDAS): Utilizing multiple GCIP products and partners in a continental distributed hydrological modeling system. *J. Geophys. Res.*, **109**, D07S90, doi:10.1029/2003JD003823.
- Mo, K. C., L. N. Long, Y. Xia, S. K. Yang, J. E. Schemm, and M. B. Ek, 2011: Drought indices based on the Climate Forecast System Reanalysis and ensemble NLDAS. *J. Hydrometeorol.*, **12**, 181–205.
- , L. Chen, S. Shukla, T. J. Bohn, and D. P. Lettenmaier, 2012: Uncertainties in North American Land Data Assimilation Systems over the contiguous United States. *J. Hydrometeorol.*, **13**, 996–1009.
- Mu, Q., M. Zhao, J. S. Kimball, N. G. McDowell, and S. W. Running, 2013: A remotely sensed global terrestrial drought severity index. *Bull. Amer. Meteor. Soc.*, **94**, 83–98.
- Priestley, C. H. B., and R. J. Taylor, 1972: On the assessment of surface heat flux and evaporation using large-scale parameters. *Mon. Wea. Rev.*, **100**, 81–92.
- Ryu, Y., and Coauthors, 2012: On the temporal upscaling of evapotranspiration from instantaneous remote sensing measurements to 8-day mean daily-sums. *Agric. For. Meteorol.*, **152**, 212–222.
- Savitzky, A., and M. J. E. Golay, 1964: Smoothing and differentiation of data by simplified least squares procedures. *Anal. Chem.*, **36**, 1627–1639.
- Schaake, J. C., and Coauthors, 2004: An intercomparison of soil moisture fields in the North American Land Data Assimilation System (NLDAS). *J. Geophys. Res.*, **109**, D01S90, doi:10.1029/2002JD003309.
- Schreiner, A. J., S. A. Ackerman, and B. A. Baum, 2007: A multispectral technique for detecting low-level cloudiness near sunrise. *J. Atmos. Oceanic Technol.*, **24**, 1800–1810.
- Sheffield, J., Y. Xia, L. Luo, E. F. Wood, M. B. Ek, and K. E. Mitchell, 2012: North American Land Data Assimilation System: A framework for merging model and satellite data for improved drought monitoring. *Remote Sensing of Drought: Innovative Monitoring Approaches*, B. D. Wardlow, M. C. Anderson, and J. P. Verdin, Eds., CRC Press, 227–260.
- Svoboda, M., and Coauthors, 2002: The Drought Monitor. *Bull. Amer. Meteor. Soc.*, **83**, 1181–1190.
- Wei, H., Y. Xia, K. E. Mitchell, and M. B. Ek, 2013: Improvement of the Noah land surface model for warm season processes: Evaluation of water and energy flux simulation. *Hydrol. Processes*, **27**, 297–303, doi:10.1002/hyp.9214.
- Xia, Y., M. B. Ek, H. Wei, and J. Meng, 2012a: Comparative analysis of relationships between NLDAS-2 forcings and model outputs. *Hydrol. Processes*, **26**, 467–474.
- , and Coauthors, 2012b: Continental-scale water and energy flux analysis and validation of the North American Land Data Assimilation System project phase 2 (NLDAS-2): 1. Intercomparison and application of model products. *J. Geophys. Res.*, **117**, D03109, doi:10.1029/2011JD016048.